University of Alberta

DIELECTROPHORESIS IN SURFACE FOULING PREVENTION

by

Tathagata Chakraborty

A thesis submitted to the Faculty of Graduate Studies and Research
in partial fulfillment of the requirements for the degree of

Master of Science

Department of Mechanical Engineering

Fall 2011
Edmonton, Alberta

Abstract

AC Dielectrophoresis, the motion of dielectric colloidal particles in the presence of an inhomogeneous AC electric field, has been utilized in this work as a mechanism for preventing channel wall fouling due to particle deposition for a multi-component colloidal system. Both attractive and repulsive DEP force fields were examined in aqueous suspensions of silica and polystyrene particles. Under a continuous cross-flow condition in a rectangular channel, particle movement away from the channel wall was visualized when a repulsive DEP force field was applied. In order to achieve a cleaner channel wall, the effect of various parameters, such as, frequency and amplitude of the AC signal, cross flow velocity, particle size and density on the particle levitation were investigated for both single-component and binary colloidal suspensions. The results also depict that the levitation of the individual species can be further controlled in order to achieve selective adsorption or field flow fractionation.

Acknowledgements

To my parents and brother for whom this is a dream come true. My supervisor Dr. Subir Bhattacharjee, who has been more than a beacon of inspiration and also guiding me through various challenges that I had faced for the entire duration in my Masters. I always came to him burdened with problems and he was always forthcoming to solve them, be it in the professional or personal front. A long discussion with him would always keep me charged up for the entire day when I searched for solutions in research. Most important of all, his optimism and energy led me to believe in myself when I doubted my own abilities. His painstaking efforts in correcting my papers thoroughly motivated me to be a perfectionist and I still fail to comprehend the source of his unabated enthusiasm. I hope someday I would really succeed to imbibe the kind of love and dedication that he puts in his work, and for which he will always have my greatest respect. Without his constant support and supervision, it would not have been possible for me to complete this treatise. To Reeshav, for hearing my endless ramblings and converting them to comprehensible numerical codes. To Arnab, for calming me down with a few soothing words when I could not see any light at the end of the tunnel. To Jim, who taught me the secrets of fabrication. To Naga Sivakumar Gunda, who has been a role model as a researcher and always forthcoming in discussions of dielectrophoresis over a cup of coffee. To all my friends in the NINT 6th floor who were with me when I was into the most difficult phases. To all my school friends and family who ultimately believed in me and made me realize my mistakes and achievements. In the end, This thesis is dedicated specially to my mother for whom I do everything in life and who has taught me to strive to be a better human being

wherever I may be.

Contents

List of Tables

List of Figures

Nomenclature

ϕ	Electric potential, V
W	Width of the electrode, m
G	Gap of the electrode, m
a_j	Leading edge of the j^{th} electrode, m
b_j	Trailing edge of the j^{th} electrode, m
$\mathbf{F_{DEP}}$	Norm of the DEP force, N
$\mathbf{F_{Drag}}$	Stokes' drag force, N
$\mathbf{F_{DEP,x}}$	X-component of DEP force, N
$\mathbf{F_{DEP,y}}$	Y-component of DEP force, N
$\mathbf{F_g}$	Gravity force, N
$\mathbf{E}$	Norm of the electric field, V/m
$\mathbf{E_x}$	X-component of the electric field, V/m
$\mathbf{E_y}$	Y-component of the electric field, V/m
$K(\epsilon_{p^*}, \epsilon_{m^*})$	Clausius-Mossotti factor
$Re(K(\epsilon_{p^*}, \epsilon_{m^*}))$	Real part of Clausius-Mossotti factor
$\mathbf{v_x}$	Cross flow velocity, m/s
$\mathbf{u_m}$	Migration velocity of the particle, m/s
$\mathbf{u}$	X-component of migration velocity of the particle, m/s
$\mathbf{v}$	Y-component of migration velocity of the particle, m/s
a	Radius of the particle, m
v	Volume of the spherical particle, m^3
ρ_p	Density of the particle, Kg/m^3
ρ_m	Density of the medium, Kg/m^3
η	Viscosity of the medium $Pa - s$
ϵ_0	Permittivity of free space, Fm^{-1}
X, Y	Axial and transverse directions of the considered Cartesian coordinate system

Chapter 1

Introduction

1.1 Background

Fouling refers to the deposition of undesirable surrounding material leading to encrustment of a surface thereby increasing the cost of operation and reducing the operating life of the equipment. Fouling adversely impacts the surfaces of various process equipment like membranes, evaporators and condensers in industries like power generation, petrochemicals and desalination plants [Epstein, 1997, Zdaniuk et al., 2006].

Fouling affects performance of heat exchangers [Falconnet et al., 2006, Molla and Bhattacharjee, 2007, Somerscales, 1990], membrane filters [Falconnet et al., 2006, Molla and Bhattacharjee, 2005], bioreactors [Yigit et al., 2009], microfluidic channels [Falconnet et al., 2006, Popat and Desai, 2004], increases drag on ship hulls [Dhanasekaran et al., 2009] and enhances scaling of oil pipelines [Flemming, 1993]. Considerable attention has been devoted to reducing fouling including use of anti fouling coatings [Liu et al., 2010, Wei et al., 2010], aggressive cleaning cycles using chemicals [Fan et al., 2008], physical methods such as use of vibration and sound [Kobayashi et al., 2003, Veerasamy et al., 2009] and electrical forces, both AC and DC [Molla and Bhattacharjee, 2007, Du et al., 2009, Liu and Cho, 1999]. However, most of the above mentioned methods have inherent disadvantages, which include generation of harmful effluents during chemical treatment, requirement of high energy in ultrasonic or physical disturbance creation mechanisms and specificity towards selective compounds (hence inability to work with multiple foulants) in systems based on chemistry or electrochemistry. This necessitates continued

demand for alternative techniques in preventing fouling of surfaces.

Combined fouling [Kim et al., 2009] by multiple species in a multi-component system is the most realistic fouling mechanism in an industrial process. This assumes major significance in colloidal fouling of membranes where the membrane surface is subjected to simultaneous fouling by a number of colloidal entities with varying physical and chemical properties. Each of these individual components exhibit different foulant-membrane interactions due to variation in surface properties such as roughness [Bico et al., 2002], surface charge [Boussu et al., 2007] and chemical anisotropies [Rosenhahn et al., 2010], leading to more complicated fouling scenarios.

Typically foulants in aqueous streams encountered in industrial practices have their dielectric constants widely different from that of the solvent (water). Capitalizing on this common difference, one can potentially target a suitable electrokinetic technique that can mitigate combined fouling.

The interaction of the induced dipoles in a colloidal particle in presence of a spatially inhomogeneous electric field gives rise to a force which may be attractive or repulsive depending on the relative polarizabiliy of the constituents of the colloidal suspension (particles and suspending medium). This force can be used in conjunction with a high frequency AC field to give rise to an electrokinetic force on the particles. This force is termed as the dielectrophoretic (DEP) force [Pohl, 1978].

From its inception [Pohl, 1978, Crews et al., 2007], the applications of dielectrophoresis was mainly limited to the areas of particle characterization [Sanchis et al., 2007], controlled drug delivery [Suehiro et al., 2008], cell separation [Yang et al., 2010] and field flow fractionation [Gascoyne et al., 2009, Peng et al., 2006]. It is only recently, that it's role in other areas as in fouling prevention is being looked into in greater detail. A novel method of membrane fouling prevention by AC dielectrophoresis was proposed by Molla and Bhattacharjee [2005] and later looked into by Du et al. [2009] in a single component fouling. However, a clear understanding of the technology in a combined fouling scenario is required for it's general applicability in industrially relevant multi-component systems and this provides the motivation behind the cur-

rent work. The principal advantage of AC dielectrophoresis is that it can act even on uncharged particles unlike DC electric fields, which require presence of charged particles. This becomes critical in scenarios of combined fouling where more than one foulant is involved, consisting of both charged and uncharged species. In this context, the efficacy of AC dielectrophoresis as a foulant removal method is investigated in this work in case of both single and multi-component fouling scenarios.

By using dielectrophoresis as the external force to levitate particles to different heights in a chamber, separation of particles is possible according to their dielectric properties and density. Experimental studies, [Markx et al., 1997, Huang et al., 1997, Rousselet et al., 1998, Wakizaka et al., 2004] showed the possibility of combining dielectrophoresis with field flow fractionation and reported the dielectrophoretic levitation to be independent of the particle size in static systems. An analytical model [Markx et al., 1997] was developed by which the particle achieved a stable levitation height under the influence of gravity and the DEP force. However, most of the previous studies focus their attention to single component and stationary systems.

As discussed earlier, the applications of dielectrophoretic levitation was mainly tailored towards biomedical applications involving isolation, identification and collection of cells. Taking a step further, in the present study we direct our efforts to combining DEP with a cross flow system, and preventing the particles in the feed suspension from depositing on the channel wall by a combination of DEP and hydrodynamic interactions. The combination of DEP, gravity and hydrodynamics can potentially lead to a tunable fouling prevention method for multi component colloidal fluids.

In the present study it is shown that, for a binary colloid suspension, with a suitable electrode array embedded on a channel wall, the repulsive (negative) DEP force would prevent settling of multiple types of colloidal particles on the wall. Also, levitation of the individual species can be controlled in order to selectively prevent adsorption of species in a multi-component system simply by varying the applied frequency or amplitude. The levitated particles could then be carried away by the tangential flow, thus preventing further deposition of particles. The levitation height measurement of colloidal particles on a

parallel electrode geometry and it's ramifications on the particle trajectory near the electrode surface in a binary colloidal suspension are then discussed in the light of a trajectory analysis model.

1.2 Objective and Scope

The objective of this study is to experimentally demonstrate the ability of DEP to levitate the particles from the channel walls in a multi-component system and to highlight the selective levitation of foulants. However, the scope of the study is currently limited to impermeable rectangular channel geometry and all the experimental and numerical results are compared within this domain. Extension of the results into practical industrial solutions will warrant further experiments by scaling up the technology to acceptable industrially relevant configurations. In addition, the current scope of research is restricted to analysis of two types of particles e.g. silica and polystyrene on a glass substrate. The analysis is typically based on a simplified model neglecting all forms of inter-particle interactions owing to the initial assumption of a dilute solution.

1.3 Organization of the Thesis

In this chapter, the scope and objective of the thesis is outlined with a brief description of the problem statement of fouling mitigation.

Chapter 2 gives a critical literature review of the problem of fouling and it's governing mechanisms. A comparative study between prevalent industrial antifouling techniques contributes to justify the significance of applying dielectrophoresis in fouling prevention, thus providing the underlying motivation of the current study.

In Chapter 3, a discussion of the governing physics behind the general phenomenon of dielectrophoresis (DEP) along with the system geometry is presented. This is followed by a detailed description of the computational geometry along with the analytical and numerical techniques used for subsequent derivation of DEP force in presence of an inhomogeneous electric field. A trajectory model for prediction of particle transport under a combination of deterministic and hydrodynamic forces has been discussed in detail.

Chapter 4 describes the details of the experimental system combined with the materials and methods utilized in the experiment. This includes device fabrication details such as the optical mask preparation and different photolithography steps. In addition, some important experimental observations of dielectrophoresis are also discussed for a single component system.

Chapter 5 mainly comprises of the results and discussions encompassing single and multi-component systems, along with the validation of the numerical trajectory analysis results with the observed experimental data.

Finally in Chapter 6, a number of relevant conclusions from the work are drawn, ending with the some suggestions for the possible future direction of research involving dielectrophoresis as a technique for prevention of surface fouling.

Chapter 2

Literature Review

2.1 Fouling of Surfaces

Typically, fouling refers to the undesirable process of encrustment of a surface while being exposed to the surrounding material [Magin et al., 2010] . Fouling of surfaces is a widely researched subject, sharing special relevance in processes associated with transport through membranes. Considerable research has been done to outline the major causes of fouling in process industries over the past decade. The current literature review broadly consists of three major parts. The first section deals with the governing mechanisms involving transport of foulants to a surface while the second part highlights the prevalent and potential fouling prevention methods. The final part of the literature review focuses on the mitigation of fouling in general and explains the rationale of selecting AC dielectrophoresis as a fouling remediation technique in light of the previous discussions.

2.2 Fouling Mechanisms

Any surface in prolonged contact with a foulant species, will cause the foulant to deposit on the surface thereby giving rise to a foulant layer. The causes and mechanisms of fouling vary widely depending on target areas, nature of foulant and operating conditions like temperature and pressure [Bell and Mueller, 2001]. A comprehensive review addressing the state of fouling science and technology highlighting the governing principles of fouling in a broader context was presented by Melo et al. [1988] and Somerscales and Knudsen [1981].

Fouling by sedimentation is by far the most common form of naturally occurring fouling process [Bell and Mueller, 2001]. This typically involves the deposition of suspended solids on an exposed surface. The suspended solids are deposited in subsequent layers, the thickness of which progressively increases with time thereby causing enhanced fouling of the surface. A comprehensive review of different fouling mechanisms including particulate fouling in heat transfer equipments is given by Somerscales and Knudsen [1981] and Epstein [1997]. A typical example of particulate fouling was further investigated by Turner and Lister [1991]. This involved the deposition of river clay on stainless steel surface dictated by sedimentation.

Apart from the aforementioned physical causes, fouling can also occur due to the associated chemical reactions in the industrial process stream occurring near the surface [Bell and Mueller, 2001]. In the chemical fouling process, it is not uncommon for a component to be firmly embedded onto the fouled surface as a result of the precipitation reactions, a process commonly known as scaling [Dalas and Koutsoukos, 1990]. An excellent review of the inorganic scaling process in pressure driven membranes is given by Shirazi et al. [2010]. The scales are mainly composed of calcium, barium and magnesium carbonates, sulphates and silicates which are present as dissolved salts in natural water. The high concentration of sulphates and carbonates subsequently engender precipitation of salts on the membrane surface when their solubility product is exceeded. The silica present in water is also one of the major contributors to inorganic fouling in desalination plants. Sheikholeslami and Tan [1999] investigated the governing mechanism, where monomeric water soluble silica crystallizes in presence of a metal hydroxide thus forming a highly insoluble metal silicate on the receptive surface. Important studies on particulate silica fouling in context of evaporators have also been highlighted [Yu et al., 2002].

Scaling can also occur based on a thermal change of the colloidal suspension. The feed stream generally contains certain dissolved salts, which exhibit a low solubility value at elevated temperatures [Bell and Mueller, 2001]. As a result, when the suspension is subjected to a temperature rise, the dissolved salts undergo crystallization at random locations which contributes to a highly resistant fouling layer. This is one of the major causes of fouling on heat exchangers by dissolved inverse solubility salts like calcium sulfate and calcium

carbonate and has been studied in detail by Bansal and Muller-Steinhagen [1993] and Kazi et al. [2010] mainly in context of evaporators and other forms of heat exchangers.

Membrane fouling still proves to be the primary factor, inhibiting use of ultrafiltration membranes in water treatment industries on a large scale due to requirement of elaborate pretreatment processes [Gao et al., 2011]. In context of membranes, reverse osmosis and nanofiltration are radically emerging as key technologies in desalination and waste water reclamation industries [Tang et al., 2011, Ning and Troyer, 2007]. Colloidal fouling, caused by accumulation of particulate matter and microorganisms proves to be a major deterrent to the efficient operation of the membrane processes [Tang et al., 2011]. The propensity of fouling of such membranes is determined by a complex interplay between the colloidal, hydrodynamic and ionic interactions in the feed suspension along with the physico-chemical properties of membrane and foulants [Tang et al., 2009, Wang and Tang, 2011]. Apart from experimental studies [Chong et al., 2008] in this field, several theoretical models have been put forward in order to explain the fouling mechanism engendered due to dissolved electrolytes in the system. These models greatly simplified the understanding of the interplay between various intermolecular forces and surface heterogeneities in hindered particle transport and pore transport of ionic solutes. These include concentration-polarization models and resistance models in membranes [Bhattacharjee et al., 1999, Chong and Fane, 2009, Chen et al., 1997]. In case of heat exchangers, the pioneering models were developed quite early by Hasson and Zahavi [1970], Epstein [1986] and Andritsos et al. [1996]. Developing on the previously described simplified models, a number of composite models for predicting the fouling rate of both crystallization and particulate fouling in heat exchangers have also been developed [Sheikholeslami, 2000]. Similar multi-component, combined fouling models have been put forward for colloid particulates, solute ions and organic matter in ultra and nanofiltration membranes [Bhattacharjee et al., 2001, Bhattacharjee and Johnston, 2002].

Combined fouling is the most realistic fouling mechanism as the process water stream normally contains more than one component, thus requiring advanced models and experimentation to properly analyze the contributions of individual mechanisms in the overall fouling behavior. An important direction

was to unify the theories for colloid, macromolecules and solute ions incorporating cake-enhanced and binary colloidal fouling models for investigation of various synergistic effects in combined fouling [Kim et al., 2009, Li and Elimelech, 2006]. The studies on combined fouling of reverse osmosis and nanofiltration membranes have been limited, since most of the earlier studies concentrated on single component fouling [Tang et al., 2011]. However, there is still a dearth of comprehensive theoretical and experimental works in complicated multi-component fouling scenarios. Therefore, critical flux based studies involving complex foulant-membrane and foulant-foulant interactions deserve greater attention in future research [Tang et al., 2011].

Biofouling in membrane reactors, reverse osmosis and ultrafiltration membranes, ship hulls and pipelines constitute an important class of fouling. By this process, bioorganisms, like bacteria, on being transported to the surface, experience rapid growth leading to the formation of a biofilm [Bell and Mueller, 2001]. Several studies have been reported [Dobretsov et al., 2006, 2009, Dhanasekaran et al., 2009] regarding the role of marine microorganisms in fouling of ship hulls and biofouling in marine biosensors [Wisniewski and Reichert, 2000, Zhao et al., 2010]. Marine antifouling techniques have evolved a long way from use of environmentally detrimental biocidal compounds to development of non toxic antifouling strategies. These strategies involve investigating into a broad range of physico-chemical attributes like surface roughness and surface chemistry, the combination of which plays a critical role for inhibiting surface fouling caused by biological organisms and their by-products [Magin et al., 2010]. Combined with these, the hydrodynamic interactions [Lauga and Powers, 2009] and surface energy can also contribute significantly to the overall fouling behavior of marine micro-organisms. However, most of the above studies focus on the role of topographical [Bico et al., 2002] and chemical anisotropy [Rosenhahn et al., 2010] on surface fouling, which consequently provided the incentive to further exploration of the effects of electrical heterogeneity on preventing particle attachment to surfaces. At present, the absence of an universally applicable antifouling strategy has initiated further research towards development of broadly effective antifouling techniques, tailored toward prevention of biofouling involving a complex mixture of foulants [Magin et al., 2010].

Microfluidic channels are important in many areas, mainly related to biochemistry like cell-based assays [Barbulovic et al., 2008] in microbiology and in biomedical engineering for analytical and therapeutic reasons like gas embolotherapy [Qamar et al., 2010]. Microchannels have numerous applications, specially in the domain of mixing and emulsions [Chang and Su, 2008] and chemical reactions for drug delivery [Santini Jr. et al., 2000]. The biggest challenge at present is the undesirable biofouling that occurs due to the accumulation of negatively charged foulants in the inner surface of the channel.

For the mitigation of the above problem of biofouling, a variety of techniques like oxygen plasma treatment [Tan et al., 2010], adsorbed coatings of surfactants [Hu et al., 2010] and protein or lipid coatings have been explored in great detail. At present, the focus mainly lies in the surface modification techniques to prevent the adhesion of biological cells in microfluidic systems. The plasma treatments are mostly used as they are an intrinsic part of the fabrication process of most microchannels. Chemical treatments are also very common, however chemicals tend to be aggresive and it is difficult to ensure that the microchannels have a biocompatible surface after such a treatment [Falconnet et al., 2006]. These surface treatments, however, require periodic reapplication. Thus there arises a need for a better non-invasive fouling prevention technique which does not affect the composition or concentration of the original species in the solution.

In the next section, a discussion on the different ways to prevent deposition and fouling in process equipment in different scenarios is presented.

2.3 Fouling Prevention

Fouling remediation is of primary importance in water treatment, desalination, petroleum, food-processing and agricultural industries. In this respect, the following prevalent industrial fouling remedies are discussed.

2.3.1 Chemical

The role of fouling prevention using chemicals is largely limited to irreversible fouling scenarios in which the physical methods like backwashing are not sufficient to remove the foulant. However, the use of chemical cleaning warrants extreme care and suitable understanding of the foulant species, specially in the case of membranes [Baker and Dudley, 1998]. The composition of the scaled layer is of primary importance in order to prescribe the correct dosage and type of chemical to be introduced in the system. The prevalent methods of determining the dominant foulant composition are mainly comprised of inspection by XRD (X-Ray diffraction) and SEM (Scanning electron microscopy). These techniques involve using X-rays and focussed electron beams to impinge on the surface of the fouled membrane. As a result, the different foulants adhering to the membrane generate varying electrical signals which are subsequently used to identify the physical and chemical nature of the foulants attached to the membrane surface. Recent studies on the fouling inspection methods has been done in case of reverse osmosis membranes [Kwak et al., 2001].

Membrane fouling is found to be alleviated to a great extent by pretreatment of the feed suspension and effective monitoring and control of the underlying process parameters, by employing techniques like acidification, softening, prefiltration and addition of surfactant and other chemical agents [Gao et al., 2011]. The common pretreatment options mostly used are coagulation, adsorption, oxidation and biological treatment [Gao et al., 2011]. The scaling deposits are generally removed by acids or by EDTA (ethylenediaminetetraacetic acid). Normally, acidification is used for preventing inorganic fouling whereas alkali solutions are prevalent against fouling by organic matter [Gao et al., 2011]. As discussed previously, the effective execution of chemical cleaning requires extensive knowledge of the dominant foulant in the process water stream. Furthermore, generation of harmful industrial effluents and strict regulations for proper disposal techniques are the current drawbacks of this method [Gao et al., 2011].

2.3.2 Mechanical

The physical methods are used to remove fouling from a surface as long as the fouling is reversible. In underwater ship hulls, it is the prevalent method to

apply rotary scrubbers to clean the deposited biofoulant layers. However, the use of other methods such as water jet removal is warranted for delicate finned structures where mechanical scrubbing may alter the design of critical components. The simplest method for non-invasive foulant removal in membranes is still by simple backwashing which has been studied in detail [Yigit et al., 2009].

Membrane rinsing mainly consists of both backwashing and forward flushing, both of which are effective in removing particulate matter from the membrane surface. However, the exact selection of rinsing methods to be used depends largely on the fouling mechanisms and nature of foulants [Gao et al., 2011]. One such study has shown the preferability of backwashing method when applied to sodium alginate fouling rather than humic acid fouling [Katsoufidou et al., 2008, Gao et al., 2011]. Most importantly, membrane fouling can be considerably reduced by rinsing under optimized process parameters such as velocity and pressure. In addition, the application of a suitable cross flow velocity on the membrane surface has significantly reduced fouling [Smith et al., 2006].

Enhanced shear flow techniques like air scouring of membrane surfaces are being used to allow sufficient momentum to the particulate matter adhering to the membrane. This becomes critical in high pressure operations which is more susceptible to causing fouling due to forced accumulation or compaction of foulants near the membrane surface [Gao et al., 2011]. However, there is still need for comprehensive literary work supporting this technique as it is still largely under development. Precise control over the critical process variables such as size and frequency of the air bubbles in the fluid suspension can lead to perfecting this nascent technique into a full fledged foulant removal method [Gao et al., 2011].

2.3.3 Ultrasonic

In the field of membranes, the method of ultrasonication in reverse osmosis membranes has been studied extensively [Feng et al., 2006] for treating waste water effluents. Similar studies have been put forward [Veerasamy et al., 2009] for natural rubber skimming by ultrafiltration membranes including detailed reviews on the enhancement of filtration by ultrasound method [Kyllonen et al., 2005]. The mechanism of ultrasonic removal involves vibrating the membrane

by application of an ultrasonic wave which imparts physical motion to the foulants sitting on the membrane. The engendered mechanical vibrations dislodge the foulant from the membrane surface thus preventing further fouling or scaling. The major drawbacks of ultrasonic method of fouling prevention are, mechanical ruptures of membrane due to prolonged operation and associated high energy input cost.

2.3.4 Magnetic

Magnetic methods of scaling prevention has been in use in the process industries for a considerable period of time. However, this method of scale prevention has generated lot of dispute in the industrial sectors on account of various conflicting theories. A detailed review of this anti-fouling technology have aimed at explaining the fouling behavior by the combination of various interionic and interfacial forces has been given by Baker and Judd [1996]. The research however, is in it's infancy and the exact mechanism behind this novel scale reduction technique still remains elusive.

2.3.5 Electrical

Electrical methods have been used in the industry for quite some time, though their efficiency has been controversial. However, [Lee and Cho, 2002, Cho et al., 2004, Van Hulle et al., 2007] a number of other groups have shown that the method was successful in preventing fouling in pilot scale heat exchanger tubes to a considerable extent. This area is still the subject of intense research. Furthermore, numerous research groups [Cho et al., 1997] [Sohn et al., 2005] investigated the feasibility of electronic descaling techniques using solenoids. This involves use of solenoids around tube sections carrying the feed suspension. When an electrical signal is applied to the solenoid it creates a magnetic field, which in turn generates an electric field in the suspension [Liu and Cho, 1999]. The action of the electric field on the mineral ions mitigates the hard scale formation. However, these techniques are still under investigation and mostly limited to single component fouling mitigation. The effectiveness of these techniques in dealing with complex mixture of foulants still needs to be verified.

2.3.6 Other Methods

A deviation from the above methodologies have managed to draw attention towards unconventional forms of fouling prevention. Novel methods such as anti-fouling coatings on heat exchangers have been studied in detail [Dowling et al., 2010]. Apart from these, there has been a renewed interest in the modification of surfaces especially [Jelvestam et al., 2003] [Xiong and Liu, 2010] in the field of biomimetic materials and biological control of membrane biofouling. Earlier means of preventing biofouling generally involved modifying the surfaces with functional materials for release of biocidal agents like silver, quaternary ammonium salts for degrading the micro-organisms causing fouling [Banerjee et al., 2011]. These coatings have inherent limitations of non-activity and deplete away after prolonged use. With increased restrictions on application of biocidal agents, antifouling coatings of PEG (poly ethylene glycol) and surface topographical approach for imparting adhesion resistance against micro-organisms have assumed greater importance [Banerjee et al., 2011]. One such modification technique includes plasma treatment of an exposed surface. Despite the encouraging results, such a technique would not be feasible for real life large scale marine applications due to size constraint of the plasma process and is currently limited to *in-situ* sterilization of biomaterials [Bazaka et al., 2011].

Significant improvements in modification of membrane surfaces is proving to be another important foulant removal technique in wastewater industries. The techniques that deserve special mention include surface coating, grafting and implantation of antibacterial agents on membranes [Tang et al., 2011, Yang et al., 2009]. PVA coated reverse osmosis membranes have been shown to display improved anti fouling properties by resisting biofilm formation [Tang et al., 2011, Lee et al., 2010], though their effectiveness is currently limited to the initial fouling stages.

2.3.7 Combined Methods

As discussed above, the causes of fouling can be varied based on the nature of the foulants. In relation to this, effort has been made to combine multiple methods in order to target different fouling mechanisms simultaneously. A recent work in this field has been reported by Liu and Cho [1999], where

a combination of the previously discussed electronic anti fouling method and mechanical abrasive method was used to mitigate tube fouling in a shell and tube heat exchanger. This essentially consists of a solenoid wrapped around a feed pipe carrying the suspension. The application of a pulsed current to the solenoid causes molecular agitations in the mineral ions and form softer scaling. This can be used in conjunction with mechanical means of fouling removal by scrubbing off the scaled layer providing enhanced fouling reduction. However, this study is mainly limited to calcium carbonate scaling and particulate fouling of heat exchangers and lack general applicability to all modes of fouling.

From the previous discussions, it has to be kept in mind that fouling can occur due to a single dominant mechanism or a combination of mechanisms, making fouling prevention all the more difficult. While there is no golden rule to mitigate all forms of fouling by a single remedy, understanding the dominant fouling mechanism and identifying the foulant composition on a specific case by case basis is warranted.

2.4 Dielectrophoresis in Fouling Prevention

Among the methods discussed in Section 2.2, the electrical method of fouling prevention is gaining renewed interest due to ease of operation, reduced maintenance and downtime. While the use of chemicals and other methods warrant constant monitoring and skilled operator use, electrical methods on the other hand, are much more simplified. Indeed, chemical methods may generate several harmful environmental effluents that pose additional problems of proper disposal and cleaning. In this respect, electrical methods provide a much cleaner operating environment. However, most of the current industrial electrical systems use direct current and utilize higher values of input voltage in the order of kiloVolts. In this light, dielectrophoresis is investigated as an alternate low energy electrokinetic method for prevention of multi-component fouling specially in context of biofouling.

Dielectrophoresis is an electrokinetic phenomenon first proposed and defined by Herbert Pohl as : the motion of a dielectric particle produced as a result of the interaction of non-uniform electric field with the effective dipole moment of the particle [Pohl, 1978, Morgan and Green, 2003]. A charged body

when placed in an external electric field, is acted upon by an electric force and experiences a movement along the electric field lines. However, when a dielectric body is placed within an electric field it undergoes spatial separation of charge known as polarization. When the applied field is uniform, there is no movement of the particle since it is acted upon by equal forces in opposite directions. In presence of an associated field inhomogeneity, the particle experiences unequal forces on the dipoles and this results in a translational motion towards the region of higher electric field depending upon the polarizabilities of the particle and the suspending medium. This force is significantly different from electrophoresis, which describes the motion of charged particles in an electric field [Morgan and Green, 2003]. The dielectrophoretic applications in different areas of particle concentration, manipulation and cell based assays is a topic undergoing extensive research at present.

In addition to prevention of fouling in general cases, dielectrophoresis introduces a reliable non-invasive technique for manipulation of bioparticles [Srivastava et al., 2011]. dielectrophoresis in particle transport in a colloidal suspension is largely dependent on the size of the colloidal particles. The effect of dielectrophoresis is better pronounced in microparticles due to it's dependence in size. The application of dielectrophoresis as a fouling prevention technique can also be very effective in prevention of fouling by bioorganisms having larger size.

The principal advantage of AC dielectrophoresis over similar DC based systems is that, it can act even on uncharged particles, unlike DC electric fields which require the presence of charged species. This becomes critical in scenarios of combined fouling which involve more than one foulant, comprising of both charged and uncharged species. In this context, the efficacy of AC dielectrophoresis as a foulant removal is investigated in the current study in different fouling scenarios. In addition, the selective adsorption of foulant is shown by which one of the components can be preferentially removed from the surface by variation of applied amplitude and frequency of the applied electrical signal. This helps in reducing the additional effort required for characterizing the composition of the dominant foulant and provides a distinct advantage over other methods of fouling remediation. Also, the use of an AC signal can create high electrical fields of the order of 10^6 V/m in microelectrode geometries

[Molla, 2004]. This can be a valuable alternative for industrial DC based systems which require a much higher amplitude for generating the same electric field. An emerging spin-off from AC dielectrophoresis approach is the concept of iDEP (insulator based DC dielectrophoresis) [Srivastava et al., 2011, Lapizco Encinas et al., 2004]. This technique can address the problems of conventional DC method by coating the electrodes with a suitable insulator. This prevents the electrodes from coming into direct contact with the fluid thus minimizing the associated drawbacks such as electrolytic effects and bubble formation. However in case of DC-iDEP, the polarization of suspended colloids typically depend upon spatial inhomogeneity created by changing the amplitude of the DC signal. In contrast, AC dielectrophoresis has the added avenue of frequency variation in concert with varying the amplitude of the applied electrical signal. This means that AC dielectrophoresis can affect particle transport in a more tunable fashion by changing the applied frequency along with the amplitude. Moreover, insulator based DEP is a nascent technology at best, and it's applications are yet to be fully understood when applied to more generic surfaces [Srivastava et al., 2011].

2.5 Summary

This chapter presents a comprehensive literature review of the underlying causes of fouling. A detailed comparative study on the different fouling mechanisms and fouling prevention techniques is outlined. In addition, a critical study of different physical and chemical anti-fouling procedures along with the state-of-art industrial fouling prevention processes are highlighted. The preceding review provides ample justification for investigating energy efficient and environmentally conducive alternative electrokinetic techniques over conventional methods for fouling remediation. AC dielectrophoresis is proposed as a non-destructive and reliable technique in context of fouling mitigation in general. The next chapter introduces the analytical and numerical simulation methodologies for the dielectrophoretic force in the considered electrode geometry. This is followed by a trajectory analysis of particles, employing a numerical subroutine in fortran for calculating the final levitation height in a cross flow scenario in presence of a deterministic DEP force.

Chapter 3

Numerical Calculation of Electric Field and Dielectrophoretic Force

3.1 Description of the Model Geometry

3.1.1 Geometry for cross flow

The schematic of the considered system geometry is depicted in Figure 3.1. The system geometry consists of a rectangular channel with the bottom surface embedded with a series of parallel interdigitated electrodes. The particles suspended in the surrounding fluid are subjected to a steady cross flow acting in the system. The axial and transverse directions in the channel geometry are represented by the X and Y directions respectively as shown in Figure 3.1(a). When the adjacent electrodes are actuated by a 180 degree phase shifted AC potential, the electric field gradients created in the micro-electrode array engender a repulsive DEP force profile, which prevents the particles from settling on the channel wall. Figure 3.1(a) shows the repulsive DEP force profile along with the hydrodynamic and gravity forces acting on the particle in the suspending medium.

3.1.2 Electrode Geometry

When a parallel electrode array embedded on the wall, is actuated by a 180 degree phase shifted AC potential, it creates a DEP force [Molla and Bhattacharjee, 2007], which imparts a migration velocity to the colloidal particle

thus levitating it from the surface of the electrode. The sinusoidal AC signals are applied at 180 degree phase difference in order to maximize the electric field gradient and thus engendering a higher value of DEP force. The above migration velocity causes the colloidal particle to lift away from the wall. A detailed view of the parallel electrode geometry with the electrode width and gap is indicated in Figure 3.1(b). Figure 3.1(c) separately highlights the bottom of the rectangular channel consisting of electrodes embedded on it's surface.

3.2 DEP Forces and Fields

On application of a spatially inhomogeneous electric field to a colloidal suspension, the induced dipoles of the constituent entities experience a force, the direction of which is determined by the relative polarizability of the medium and the particles [Molla and Bhattacharjee, 2007]. If the particle is more polarizable than the surrounding medium it moves towards a region of higher electric field. This phenomenon is termed as positive DEP. In the event of the particle being less polarizable than the medium, there is a consequent reversal in the direction of the force which pushes the particles to a lower field region. This is known as negative DEP. A conceptual view of the concept of positive and negative DEP has been illustrated in Figure 3.3.

3.2.1 Time Averaged DEP Force

Effective Dipole Moment of a Particle in an Electric Field

When a dielectric particle suspended in a medium, is acted upon by an external electric field, spatial separation of charges occur within the particle thereby creating a dipole. This is commonly known as polarization [Morgan and Green, 2003]. The dipole is referred to as induced dipole, since the dipole becomes non-existent in absence of an externally applied electric field. When the imposing electric field is uniform, the particle does not encounter any force. On the contrary, if an inhomogeneous electric field is applied, the dipole experiences a resultant force due to the force imbalance on both sides of the dipole. The engendered force is dependent on the relative polarizabilities of the particle and the medium and also on the frequency of the applied field. In case of a dielectric sphere suspended in an external medium, the effective

dipole moment ($\mathbf{p_{eff}}$) of the particle relates to the electric potential (ϕ) at any distance r from the center of the sphere in the following manner [Molla, 2004, Morgan and Green, 2003]:

$$\phi = \frac{\mathbf{p_{eff}} \cdot \mathbf{r}}{4\pi\epsilon_0 r^2} \tag{3.1}$$

The potential inside and outside the spherical particle with radius a at a distance r from the origin (center of the sphere) can be described as follows [Morgan and Green, 2003].

$$\phi_m = Ea^3 \left(\frac{\epsilon_p^* - \epsilon_m^*}{2\epsilon_m^* + \epsilon_p^*} \right) \frac{\cos\theta}{r^2} - Er\cos\theta \tag{3.2}$$

$$\phi_p = -\left(\frac{3\epsilon_m^*}{2\epsilon_m^* + \epsilon_p^*} \right) Er\cos\theta \tag{3.3}$$

A comparison of 3.1 and 3.2 yields the following expression for dipole moment of a dielectric sphere.

$$\mathbf{p_{eff}} = 4\pi\epsilon_m a^3 \left(\frac{\epsilon_p^* - \epsilon_m^*}{2\epsilon_m^* + \epsilon_p^*} \right) \mathbf{E} \tag{3.4}$$

$$\mathbf{p_{eff}} = 4\pi\epsilon_m a^3 K(\epsilon_p^*, \epsilon_m^*)\mathbf{E} \tag{3.5}$$

where ϵ_m^*, ϵ_p^* are the complex permittivities of the medium and the particle respectively, ϵ_m is the permittivity of the medium, a is the particle radius whereas $\mathbf{E}$ is the applied electric field vector. The quantity $K(\epsilon_p^*, \epsilon_m^*)$ is known as the Clausius Mossotti factor which is a frequency dependent complex quantity. It is important to note that, the above expression has been derived for an imperfect dielectric with ohmic losses, the real values of permittivities being replaced by the corresponding complex permittivities [Morgan and Green, 2003, Molla, 2004] of the particle and the medium. Thus $K(\epsilon_p^*, \epsilon_m^*)$ is essentially an alternate representation of the effective polarizability of the particle in the suspension, and is strongly influenced by the applied frequency. Hence, at low frequencies, the conductivities of the particle and medium play a central role in determining the extent of polarization. In contrast, at high frequencies, the polarization is mainly influenced by the permittivities of the particle and the surrounding medium.

Derivation of Force on a Particle in a Non-Uniform Electric Field

The effective dipole moment of a particle in an external electric field was formulated in the previous section. In light of the above discussion, this section aims at deriving the expression for the DEP force when the above particle is subjected to a non-uniform electric field. This involves investigating the effect of field non-uniformity by introducing a spatial variation to the electric field applied in the system. Following the approach of Morgan and Green [2003] and Molla [2004], the resultant force experienced by a dipole with two point charges +q and -q separated by a finite distance $\mathbf{d}$ is given as [Jones, 1995]:

$$\mathbf{F} = q\mathbf{E}(\mathbf{r} + \mathbf{d}) - q\mathbf{E}(\mathbf{r}) \tag{3.6}$$

where $\mathbf{E}(\mathbf{r} + \mathbf{d})$ and $\mathbf{E}(\mathbf{r})$ are the electric fields engendered at the respective charge locations. It should be noted that, the distance between the poles ($\mathbf{d}$) is assumed to be much smaller than $\mathbf{r}$. This is to ensure that the engendered electric field retains the same value across the dipole and does not undergo local changes. Using a Taylor's series expansion of the first term in the r.h.s of Equation 3.6 we get,

$$\mathbf{F} = q\mathbf{E}(\mathbf{r}) + q(\mathbf{d} \cdot \nabla)\mathbf{E}(\mathbf{r}) + HigherOrderTerms - q\mathbf{E}(\mathbf{r}) \tag{3.7}$$

Since the product $q\mathbf{d}$ represents the dipole moment of the particle, hence the expression takes the form of,

$$\mathbf{F_{DEP}} = (\mathbf{p_{eff}} \cdot \nabla)\mathbf{E} \tag{3.8}$$

Substituting the value of $\mathbf{p_{eff}}$ from Equation 3.5, to the Equation 3.8, the final expression for DEP force is derived in a non-uniform electric field. The time averaged DEP force engendered in the electrode array is thus given as [Pohl, 1978, Jones, 1995] :

$$\mathbf{F_{DEP}} = 2\pi a^3 \epsilon_m Re[K(\epsilon_p^*, \epsilon_m^*)]\nabla(\mathbf{E} \cdot \mathbf{E}) \tag{3.9}$$

where $\mathbf{E}$ is the resultant electric field, a is the particle radius, ϵ_m is the permittivity of the medium and $Re[K(\epsilon_p^*, \epsilon_m^*)]$ is the real part of the complex Clausius-Mossotti factor [Morgan and Green, 2003]. The real part of $K(\epsilon_p^*, \epsilon_m^*)$ is frequency dependent with a value typically ranging between -0.5 to +1 [Morgan and Green, 2003]. As most colloidal particles in an aqueous suspension

have a lower permittivity than water, they exhibit negative DEP at a high frequency range [Molla and Bhattacharjee, 2005]. A graph showing the variation of the Clausius-Mossotti factor of silica particle in water with the applied frequency is provided in Figure 3.4. Thus, from the above expression it is clear that, the DEP force cannot exist in presence of a uniform electric field but essentially requires a certain degree of field inhomogeneity to manifest itself.

DEP Force in Presence of a Time varying Electric Field

In the previous section, the DEP force was calculated in presence of a non-uniform electric field. Indeed, this non uniformity is further explored by considering an AC electric field where the applied signal varies with time with a constant phase lag. The approach by Morgan and Green [2003] is utilized here, whereby the behavior of the entire system can be summed up by representing the individual system variables as phasors. The potential and electric field engendered in the system is thus represented in the form of the following phasors [Molla, 2004, Morgan and Green, 2003]:

$$\phi(x,t) = Re[\tilde{\phi(x)}e^{i\omega t} \tag{3.10}$$

$$\mathbf{E}(\mathbf{x},\mathbf{t}) = Re[\tilde{\mathbf{E}(\mathbf{x})}e^{i\omega t} \tag{3.11}$$

In the Equations 3.10 and 3.11, the $\tilde{\phi(x)}$ and $\tilde{\mathbf{E}(\mathbf{x})}$ denote the complex phasors representing the potential and electric field respectively. However, in the present case with a single applied frequency with a constant phase lag, the above phasors can be reasonably considered as real quantities and the electric field becomes $\tilde{\mathbf{E}(\mathbf{x})} = \mathbf{E}$.

Rearranging the original Equation 3.5, the dipole moment is now obtained as the function of the particle volume v and the effective complex polarizability $\tilde{\alpha}$ of the particle with respect to the medium. Here $\tilde{\mathbf{p_{eff}}}$ denotes the effective complex dipole moment [Molla, 2004].

$$\tilde{\mathbf{p_{eff}}} = v\tilde{\alpha}\mathbf{E}e^{i\omega t} \tag{3.12}$$

This leads to formulation of the time averaged DEP force as,

$$< \mathbf{F_{DEP}} >= \frac{1}{2}Re[(\tilde{\mathbf{p_{eff}}} \cdot \nabla)\mathbf{E}^* \tag{3.13}$$

In the above expression, $\mathbf{E}^*$ is the complex conjugate which in this case can be replaced by a real quantity as discussed previously [Molla, 2004]. Thus the final expression becomes,

$$< \mathbf{F_{DEP}} >= \frac{1}{2} v Re[\tilde{\alpha}](\mathbf{E} \cdot \nabla \mathbf{E}) \tag{3.14}$$

The equation can be suitably modified by using the laws of vector identity to yield the governing equation for DEP force in presence of an AC electric field.

$$< \mathbf{F_{DEP}} >= \frac{1}{4} v Re[\tilde{\alpha}] \nabla (\mathbf{E} \cdot \mathbf{E}) \tag{3.15}$$

$$< \mathbf{F_{DEP}} >= \frac{1}{2} v Re[\tilde{\alpha}] \nabla |\mathbf{E}|^2 \tag{3.16}$$

In the above Equation 3.16, $\mathbf{E}$ is the root mean square value of the applied electric field and the other symbols have the same meaning as previous.

3.2.2 Analytical Formulation

In this section, a complete analysis of the electric field gradients and DEP force profile on the parallel electrode array geometry was done with the aid of Green's half plane function.

The Green's theorem method is based on the approach outlined by Clague and Wheeler [2005]. The analytic model described in this approach, enables us to find the particular solution of each and every point in the electrode geometry. The Half plane Green's function solution as elucidated by Clague and Wheeler [2005], is applied for the parallel electrode geometry already discussed above. In the footsteps of the solution provided by Clague and Wheeler [2005], a potential function can be represented with the help of an auxiliary Green's function as follows [Molla, 2004]:

$$\phi(x, y) = \int_{-\infty}^{+\infty} G(x, y|\xi) \phi_s(\xi) d\xi \tag{3.17}$$

$$G(x, y|\xi) = \frac{y/\pi}{(x - \xi)^2 + y^2} \tag{3.18}$$

where $G(x, y|\xi)$ is the auxiliary Green's function and $\phi_s(\xi)$ is the potential at a specified position on the electrode surface. The defined Green's function can be integrated in a piecewise manner to yield the net potential over the electrode plane. For simplification of the geometry, the electrodes extend to

infinity along the electrode plane thereby rendering the problem into a two dimensional one. Also the thickness of the electrodes have been assumed to be negligible that consequently simplifies the equations for potential and field on the electrode plane. The potential applied to the consecutive electrodes in the considered electrode geometry can be expressed as follows [Clague and Wheeler, 2005, Molla, 2004],

$$\phi_e(\xi) = V_0 \cos\left(\omega t + \frac{2\pi j}{n}\right) \tag{3.19}$$

where V_0 is the rms (root mean square) value of the applied amplitude, ω is the angular frequency and j represents the j^{th} electrode along the electrode plane. Here the value of n has been fixed at 2 since the DEP is stationary wave. Following the above argument, the potential between the adjacent gaps between the electrodes at a particular x value namely, x = ξ can be written as [Molla, 2004],

$$\begin{aligned}
\phi_g(\xi) &= V_0\left(\left[\frac{\cos_{j+1}-\cos_j}{2d-W}\right]\left[x-\left(\lambda_k - d + \frac{W}{2}\right)\right] + \cos_j\right) \\
\phi_g(\xi) &= C_1 + C_2 x + C_3 \\
C1 &= V_0 \cos_j \\
C_2 &= V_0\left(\frac{\cos_{j+1}-\cos_j}{2d-W}\right) \\
C_3 &= -(\lambda_k - d + \frac{W}{2})C_2
\end{aligned} \tag{3.20}$$

where λ_k denotes the center between the j^{th} and $(j+1)^{th}$ electrodes as indicated in Figure 3.2 and C_1, C_2 and C_3 are respective constants. The total potential on the electrode array at any position is given by the summation of the electrode and gap potentials over the entire length of electrode array consisting of 'N' number of electrodes [Molla, 2004].

$$\begin{aligned}
\phi(x,y) &= -\frac{1}{\pi}\sum_{j=1}^{N}\phi_e(\xi)\left(arctan\left[\frac{x-b_j}{y}\right] - arctan\left[\frac{x-a_j}{y}\right]\right) \\
&\quad -\frac{1}{\pi}\sum_{j=1}^{N-1}\phi_g(\xi)\left(arctan\left[\frac{x-a_{j+1}}{y}\right] - arctan\left[\frac{x-b_j}{y}\right]\right) \\
&\quad +\frac{C_2 y}{2}\left[ln\left(1+\left[\frac{x-a_{j+1}}{y^2}\right]\right) - ln\left(1+\left[\frac{x-b_j}{y^2}\right]\right)\right]
\end{aligned} \tag{3.21}$$

where a_j and b_j represent the leading and the trailing edges of the j^{th} electrode. Once the surface and gap potential expressions were obtained, the same can be

used to evaluate the electric fields along the electrode plane and perpendicular to it [Molla, 2004].

$$\begin{aligned} E_x &= \frac{1}{\pi}\sum_{j=1}^{N}\phi_e\left(\frac{y}{y^2+[x-b_j]^2}-\frac{y}{y^2+[x-a_j]^2}\right) \\ &+\frac{1}{\pi}\sum_{j=1}^{N-1}\phi_g(x)\left[\frac{y}{y^2+(x-a_{j+1})^2}-\frac{y}{y^2+(x-b_j)^2}\right] \\ &+C_2\left(arctan\left[\frac{x-a_{j+1}}{y}\right]-arctan\left[\frac{x-b_j}{y}\right]\right) \\ &-C_2 y\left[\frac{x-a_{j+1}}{y^2+(x-a_{j+1})^2}-\frac{x-b_j}{y^2+(x-b_j)^2}\right] \end{aligned} \tag{3.22}$$

$$\begin{aligned} E_y &= \frac{1}{\pi}\sum_{j=1}^{N}\phi_e\left(\frac{x-a_j}{y^2+[x-a_j]^2}-\frac{x-b_j}{y^2+[x-b_j]^2}\right) \\ &+\frac{1}{\pi}\sum_{j=1}^{N-1}\phi_g(x)\left[\frac{x-b_j}{y^2+(x-b_j)^2}-\frac{x-a_{j+1}}{y^2+(x-a_{j+1})^2}\right] \\ &-C_2 y^2\left[\frac{1}{y^2+(x-a_{j+1})^2}-\frac{1}{y^2+(x-b_j)^2}\right] \\ &\frac{-C_2}{2}ln\left[\frac{y^2+(x-a_{j+1})^2}{y^2+(x-b_j)^2}\right] \end{aligned} \tag{3.23}$$

Here E_x and E_y are the electric field components along X and Y directions as described in Figure 3.2. The electric field values and their gradients thus obtained over the entire array of the electrodes is then used to find the corresponding force values at respective locations.

The gradients of the field along axial and transverse directions are derived by utilizing the partial derivatives of the electric field derived earlier in Equations 3.22 and 3.23 [Molla, 2004].

$$\begin{aligned} \frac{\partial E_x}{\partial x} &= \frac{2y}{\pi}\sum_{j=1}^{N}\phi_e\left(\frac{x-a_j}{[y^2+[x-a_j]^2]^2}-\frac{x-b_j}{[y^2+[x-b_j]^2]^2}\right) \\ &+\frac{1}{\pi}\sum_{j=1}^{N-1}2y\phi_g(x)\left[\frac{x-b_j}{[y^2+(x-b_j)^2]^2}-\frac{x-a_{j+1}}{[y^2+(x-a_{j+1})^2]^2}\right] \\ &+2C_2\left(\left[\frac{y}{y^2+(x-a_{j+1})^2}\right]-\left[\frac{y}{y^2+(x-b_j)^2}\right]\right) \\ &-C_2 y\left[\frac{y^2-(x-a_{j+1})^2}{[y^2+(x-a_{j+1})^2]^2}-\frac{y^2-(x-b_j)^2}{(y^2+(x-b_j)^2)^2}\right] \end{aligned} \tag{3.24}$$

$$\begin{aligned}\frac{\partial E_y}{\partial y} &= \frac{2y}{\pi}\sum_{j=1}^{N}\phi_e\left(\frac{x-b_j}{[y^2+[x-b_j]^2]^2}-\frac{x-a_j}{[y^2+[x-a_j]^2]^2}\right)\\ &+\frac{1}{\pi}\sum_{j=1}^{N-1}2y\phi_g(x)\left[\frac{x-a_{j+1}}{[y^2+(x-a_{j+1})^2]^2}-\frac{x-b_j}{[y^2+(x-b_j)^2]^2}\right]\\ &-2C_2y^3\left(\left[\frac{1}{[y^2+(x-b_j)^2]^2}\right]-\left[\frac{1}{[y^2+(x-a_{j+1})^2]^2}\right]\right)\\ &-3C_2y\left[\frac{1}{(y^2+(x-a_{j+1})^2)}-\frac{1}{(y^2+(x-b_j)^2)}\right] \qquad (3.25)\end{aligned}$$

$$\begin{aligned}\frac{\partial E_y}{\partial x} &= \frac{1}{\pi}\sum_{j=1}^{N}\phi_e\left(\frac{y^2-(x-a_j)^2}{[y^2+[x-a_j]^2]^2}-\frac{y^2-(x-b_j)^2}{[y^2+[x-b_j]^2]^2}\right)\\ &+\frac{1}{\pi}\sum_{j=1}^{N-1}2y\phi_g(x)\left[\frac{y^2-(x-b_j)^2}{[y^2+(x-b_j)^2]^2}-\frac{y^2-(x-a_{j+1})^2}{[y^2+(x-a_{j+1})^2]^2}\right]\\ &+2C_2\left(\left[\frac{(x-b_j)}{[y^2+(x-b_j)^2]}\right]-\left[\frac{(x-a_{j+1})}{[y^2+(x-a_{j+1})^2]}\right]\right)\\ &-2C_2y^3\left[\frac{(x-b_j)}{[y^2+(x-b_j)^2]^2}-\frac{x-a_{j+1}}{(y^2+(x-a_{j+1})^2)}\right] \qquad (3.26)\end{aligned}$$

$$\frac{\partial E_x}{\partial y} = \frac{\partial E_y}{\partial x} \qquad (3.27)$$

With the above expressions for the electric field and their gradients, an analytic formulation of the DEP force can be developed. The term $\nabla(\mathbf{E}.\mathbf{E})$ in the Equation 3.9 is expressed in terms of the derivatives of the electric field along X and Y directions [Molla, 2004].

$$\frac{\partial(\mathbf{E}\cdot\mathbf{E})}{\partial x} = 2\left(E_x\frac{\partial E_x}{\partial x}+E_y\frac{\partial E_y}{\partial x}\right) \qquad (3.28)$$

$$\frac{\partial(\mathbf{E}\cdot\mathbf{E})}{\partial y} = 2\left(E_x\frac{\partial E_x}{\partial y}+E_y\frac{\partial E_y}{\partial y}\right) \qquad (3.29)$$

The field and their respective gradients can be utilized from Equations 3.22, 3.23, 3.24, 3.25, 3.26 and the axial and transverse components of DEP force can be calculated as follows [Molla, 2004]:

$$\mathbf{F_{DEP,x}} = 2\pi a^3\epsilon_m Re[K(\epsilon_p^*,\epsilon_m^*)]\frac{\partial(\mathbf{E}\cdot\mathbf{E})}{\partial x} \qquad (3.30)$$

$$\mathbf{F_{DEP,y}} = 2\pi a^3 \epsilon_m Re[K(\epsilon_p^*, \epsilon_m^*)] \frac{\partial(\mathbf{E} \cdot \mathbf{E})}{\partial y} \tag{3.31}$$

The force values obtained analytically for the requisite electrode geometry has been analyzed in detail in the 'Results and Discussions' section. In the following section, the methodology for the finite element solution of the governing Laplace equation in the electrode geometry has been discussed.

3.2.3 Finite Element Solution

The above approach of finding the exact solution by analytical method is not feasible in complex electrode geometries [Molla, 2004]. Therefore, we applied numerical methods to find the values of field and forces. The numerical simulations allow greater applicability in diverse electrode geometries, while the analytical solution purely serves as a natural placeholder verifying the correctness of the numerical model, thereby facilitating use of numerical equations in continuum or trajectory analysis. For the numerical simulations, a finite element solution of the governing Laplace equation is utilized. The previously described problem geometry along with boundary conditions elucidated in Equations 3.32a - 3.32e, is solved using a commercial finite element package, COMSOL 3.5a. A typical finite element simulation result of the resulting electric potential in the considered electrode geometry is shown in Figure 3.5.

Numerical simulations are carried out using the computational geometry as described in Figure 3.1(b). The width of the channel is considerably larger than the channel height. Based on this assumption, the geometry can be simplified to a 2D Cartesian representation of the three dimensional rectangular channel. The bottom of the channel is impermeable and consists of interdigitated electrodes as demonstrated in Figure 3.1(c). Since the DEP force follows a perfectly periodic force profile along the electrode array, a representative array section consisting of a single electrode pair is considered for the numerical solution [Molla, 2004]. The width (W) and the gap (G) between the electrodes are both set to be equal. The height of the computational domain is assumed to be four times the electrode width (H=4W), sufficient to incorporate the entire extent of the repulsive DEP force field. In absence of any free charges, the

Laplace equation along with the boundary conditions for the computational geometry are described as follows [Molla, 2004]:

$$\nabla^2 \phi = 0 \tag{3.32a}$$

$$\phi = \phi_e / V_0 = \pm 1 \qquad \delta\lambda \in W \tag{3.32b}$$

$$\phi = \phi_g / V_0 = 0 \qquad \delta\lambda \in G \tag{3.32c}$$

$$\phi = 0 \qquad \text{at} \quad 0 < x < L \quad \text{and} \quad y = H \tag{3.32d}$$

$$\nabla\phi = 0 \ \text{(Symmetry)} \ \text{at} \quad x = 0 \quad \text{and} \quad x = L \tag{3.32e}$$

where ϕ_e and ϕ_g are the applied potentials at the electrodes and the gap, and V_0 is the root mean square (rms) value of the applied amplitude. The parameter $\delta\lambda$ represents the bottom surface of the considered domain as shown in Figure 3.1(b). All the lengths are normalized with respect to the electrode width. The potential applied to the electrodes is scaled by the rms value of the AC amplitude as described in Equations 3.32b and 3.32c. The potential is assumed to vary linearly between two consecutive electrodes, having zero value at the midpoint of the electrode gap. Furthermore, the top boundary is grounded and symmetry condition is applied at the inlet and exit boundaries of the computational domain as depicted in Equations 3.32d and 3.32e.

3.3 Trajectory analysis

A trajectory analysis was also done in order to quantitatively explore the behavior of the colloidal particles in the system and to better interpret the experimental results in context of the particle behavior obtained from the simulations. A schematic of the trajectory of a single particle in the considered system is shown in Figure 3.6. Figure 3.6(a) depicts the deposition of the particle on the rectangular channel in presence of the cross flow. Figure 3.6(b) on the other hand, describes the particle trajectory when acted upon simultaneously by the repulsive DEP force field and the cross flow thereby mitigating any deposition on the surface.

3.3.1 Trajectory Equations

Trajectory of a single particle in the suspension is modeled to predict the behavior of colloidal particles in the system, and to gain physical insight into

experimental results in light of model predictions. The fluid is assumed to flow with fully developed laminar flow profile. Neglecting all other forms of inter particle interactions, the particle is subjected to hydrodynamic, gravity and dielectrophoretic forces. The motion of a particle in the system can therefore be expressed in the form of Newton's second law of motion [Molla, 2004, Molla and Bhattacharjee, 2005] :

$$m\frac{d\mathbf{v_i}}{dt} = \mathbf{F_i} \tag{3.33}$$

Here m is the mass of the particle, $\mathbf{v}$ is the particle velocity with respect to the medium and 'i' represents the x and y directions of the coordinate system. At steady state, the trajectory of a non accelerating particle can be derived on simplification of the coupled trajectory equations given by Elimelech et al. [1995] [Molla, 2004, Molla and Bhattacharjee, 2005],

$$\mathbf{u} = \frac{d\mathbf{x}}{dt} = \mathbf{v_x} + \frac{\mathbf{F_{DEP,x}} + \sum \mathbf{F_x}}{6\pi\mu a} \tag{3.34}$$

$$\mathbf{v} = \frac{d\mathbf{y}}{dt} = \frac{\mathbf{F_{DEP,y}} + \sum \mathbf{F_y}}{6\pi\mu a} \tag{3.35}$$

where $\mathbf{F_{DEP,x}}$ and $\mathbf{F_{DEP,y}}$ are the components of DEP force along horizontal and vertical directions while $\mathbf{v_x}$ represents the cross flow velocity. $\sum \mathbf{F_x}$ and $\sum \mathbf{F_y}$ represent the summation of all external forces along the two coordinate axes. $\mathbf{u}$ and $\mathbf{v}$ are the axial and transverse components of the resultant migration velocity, given as $|\mathbf{u_m}| = \sqrt{|\mathbf{u}|^2 + |\mathbf{v}|^2}$.

Simultaneously solving Equations 3.34 and 3.35 yields the complete trajectory of a particle. The hydrodynamic near wall correction factors have been neglected in the simulations as they asymptotically decay with increasing separation distance from the wall. Since the primary objective is to investigate the final levitation height, the correction factors would be insignificant in the present analysis. The trajectory equations were solved by using a FORTRAN 77 program. A numerical differential algebraic equation (DAE) solver DASSL was used for obtaining the solution.

3.3.2 Trajectory Modeling Approach

The trajectory equations 3.34 and 3.35 as outlined in the previous section were solved by writing a trajectory analysis code in FORTRAN 77. A numerical

differential equation (DAE) solver subroutine called DASSL was used for the above solution. Based on the BDF (Backward differencing formula) method, this subroutine uses the method of lines to obtain solutions of differential equations. The main advantage of DASSL is in solving initial value ODES.

If an equation can be expressed in the following implicit form of $F(t, y, y') = 0$, DASSL is most effective in solving such a problem with a given initial value. DASSL has been constructed in order to solve problems with a low index with ease but can prove tedious in solving higher index value problems [Ascher and Petzold, 1998]. DASSL uses the k^{th} order backward difference approach which represents the problem in a set of linear equations. The resulting equations are then solved using Newton's method. The subroutine makes use of adaptive stepping scheme based on the stiffness of the problem encountered. As discussed earlier, DASSL gives accurate solutions based on the correctness of the initial value supplied by the user. A fairly detailed methodology of DASSL and it's advantages in initial value problems has been described by Brenan and Eleda [1989].

A flow chart with the numerical methodology is outlined in Figure 3.7. The chart explains the sequence of the numerical techniques used in this work. Firstly, a numerical model analogous to the experimental cross flow geometry was constructed using a finite element package COMSOL 3.5a. Following this, the governing Laplace equation was solved for the entire domain with the appropriate boundary conditions. To ensure the correctness and uniformity of the solution, an analytical approach based on Green's half plane function was also adopted. The analytical data thus obtained was used as a placeholder to corroborate the correctness of the numerical force and field values obtained from finite element analysis. A particle trajectory model was subsequently developed and the dielectrophoretic force values obtained from analytical results were used as input to the constructed trajectory model. The governing equations consisted of ODE's which was solved by DASSL subroutine in FORTRAN 77. In the end, the final levitation height obtained from trajectory analysis model was then used for comparison against the levitation data obtained from actual experiment.

3.3.3 Gravity and Hydrodynamic Forces

A major aspect of this work was to investigate the effect of gravity on the deposition behavior of particles. This provided the rationale behind choosing two different types of particles with varying densities for the experiments. The gravity effect becomes even more pronounced as the size of the particle becomes larger. As discussed in the previous sections, very less attention had been focussed on the effect of gravity as it had been readily calculated that, the effect of gravity can be neglected up to particle sizes of 1 μm [Molla, 2004].

Following up on this, particle sizes as high as 5 μm were chosen in the current work in order to represent realistic scenarios of fouling where the gravity forces effecting the deposition behavior cannot be neglected while framing the trajectory model. The main effort of the modeling work was concentrated in levitation of the particles and the accuracy of the model in the light of the experimental data obtained under comparable conditions. Hence, all other forces like inter-particle interactions were not considered which becomes typical of the short range interactions of the particle when it deposits on the given surface [Molla, 2004]. These forces have very less influence as one goes further away from the electrode surface where only dielectrophoretic, gravity and hydrodynamic drag forces dictate the behavior of the particle under investigation.

Again from a hydrodynamic perspective, when the particle is levitated under the action of repulsive dielectrophoretic force it encounters frictional resistance from surrounding fluid, thus experiencing a hydrodynamic drag.

The governing equation of particle motion at steady state, which incorporates the combined contributions of the repulsive DEP, viscous drag and gravity is obtained as follows:

$$\mathbf{F_{DEP}} = \mathbf{F_{drag}} + \mathbf{F_g} \tag{3.36}$$

The Stokes' drag force acting on the particle can be evaluated from the following expression [Molla, 2004, Molla and Bhattacharjee, 2007]:

$$\mathbf{F_{drag}} = 6\pi\eta a\mathbf{u_m} \tag{3.37}$$

where η is the viscosity of the medium and $\mathbf{u_m}$ is the migration velocity of the particle with respect to the fluid. The gravity force on the particles has also

been considered in the model and can be expressed as :

$$\mathbf{F_g} = \frac{4}{3}\pi a^3(\rho_p - \rho_m)\mathbf{g} \tag{3.38}$$

where ρ_p and ρ_m are the densities of the particle and medium respectively. Substitution of $\mathbf{F_{drag}}$ and $\mathbf{F_g}$ from Equations 3.37 and 3.38 to Equation 3.36 results in the following expression [Molla and Bhattacharjee, 2007] :

$$\mathbf{F_{DEP}} = 6\pi\eta a\mathbf{u_m} + \frac{4}{3}\pi a^3(\rho_p - \rho_m)\mathbf{g} \tag{3.39a}$$

$$\mathbf{u_m} = a^2\left(\frac{2\pi\epsilon_m Re[K(\epsilon_p^*, \epsilon_m^*)]\nabla(\mathbf{E}\cdot\mathbf{E}) - \frac{4}{3}\pi(\rho_p - \rho_m)\mathbf{g}}{6\pi\eta}\right) \tag{3.39b}$$

The particle trajectory is determined by the resultant velocity field ($\mathbf{u_m}$) of the individual colloidal particles in the suspension. It is noteworthy that, the same migration velocity was discussed earlier in context of the trajectory Equations i.e. 3.34 and 3.35.

3.4 Summary

In this chapter the model geometry is discussed followed with a detailed analysis and derivation of the electrical forces in a dielectric particle in presence of a non uniform electric field. The trajectory equations for the particle have been outlined and a numerical methodology is developed for the solution of particle motion under the action of deterministic forces and an ensuing cross flow. The negative dielectrophoretic force in conjunction with the Stokes drag force and gravity force determines the resultant trajectory of the particle in the flow channel. For the sake of simplicity, the numerical model does not take into account inter-particle interactions and the electric field is considered unchanged by the presence of particles due to the initial assumption of a dilute suspension. With the previously stated assumptions, the electric field and dielectrophoretic forces are obtained numerically and later compared with the analytical results. Moreover, the particle trajectory results obtained from the trajectory analysis approach are compared with the experimental results in the subsequent chapter of Results and Discussions.

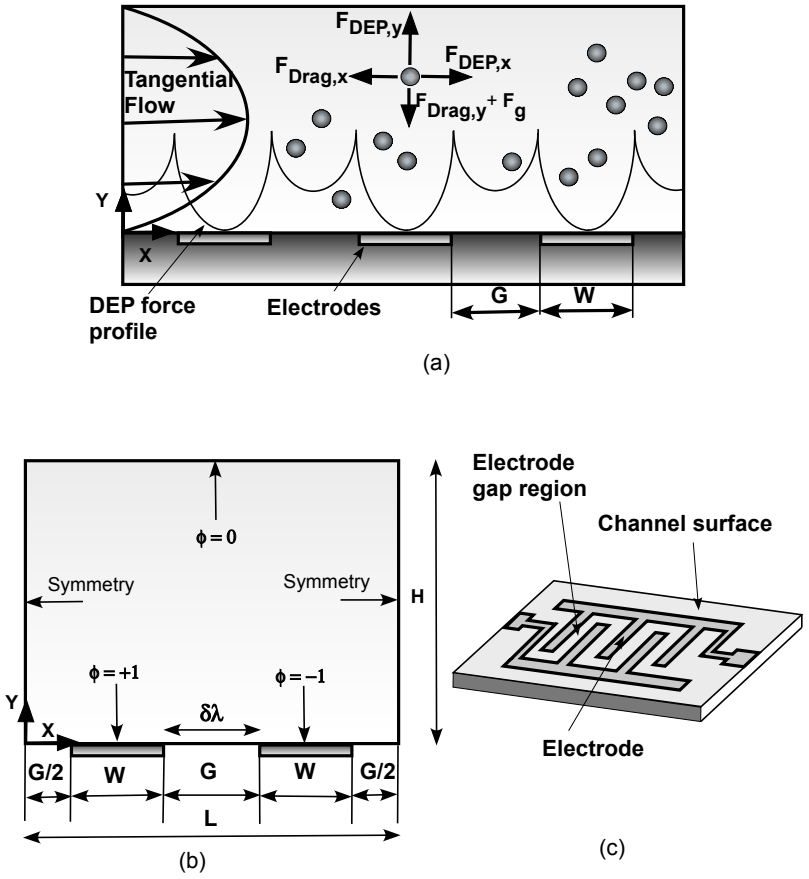

Figure 3.1 – (a) Schematic showing the system geometry depicting the repulsive DEP force profile. The particle is acted upon by the DEP forces along X and Y directions. The axial and transverse components of hydrodynamic drag force and the gravity force are also shown in the figure. (b) The computational geometry along with the applied boundary conditions is depicted. (c) The bottom surface of the channel consists of interdigitated electrodes embedded on the glass substrate with 180 degree phase shifted AC potential applied to adjacent electrodes.

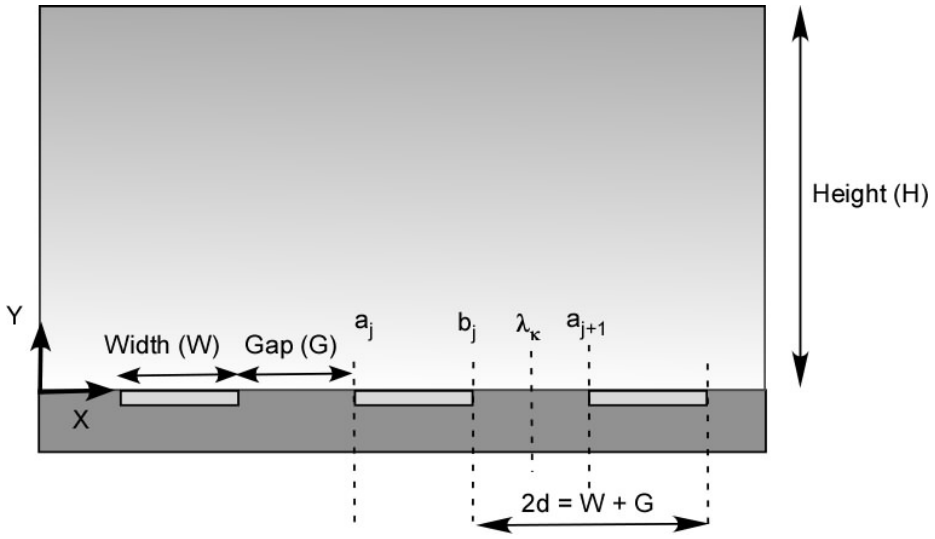

Figure 3.2 – Schematic showing a representative section of the interdigitated electrode geometry as adopted by Clague and Wheeler in their derivation for the electric field and gradients. a_j and b_j denote the leading and trailing edges of the j^{th} electrode in the electrode array. λ_k represents the mid point of the k^{th} electrode pair.

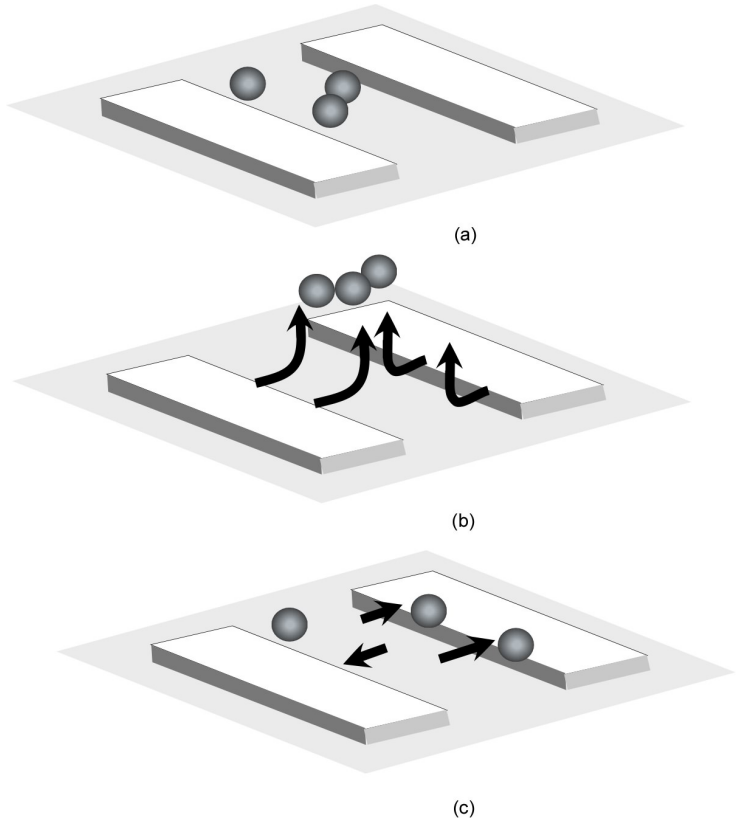

Figure 3.3 – Schematic showing the concept of negative and positive dielectrophoresis of particles, situated on an electrode array. (a) The particles roll on the surface of the electrodes. (b) The particles undergo negative DEP so that they move away and upwards from the electrode edges when AC signal is applied to the adjacent electrodes. (c) The particles experience positive DEP so that they are attracted towards the electrode edges.

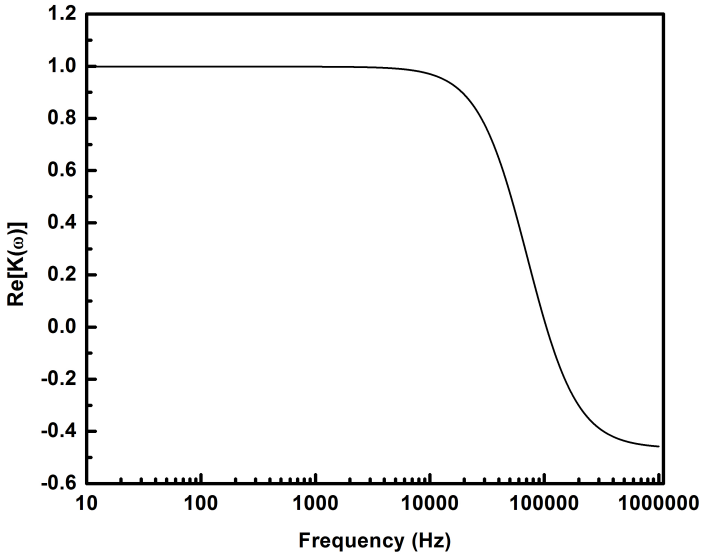

Figure 3.4 – (a)Plot showing the variation of real part of the Clausius-Mossotti factor with applied frequency for silica in water system.

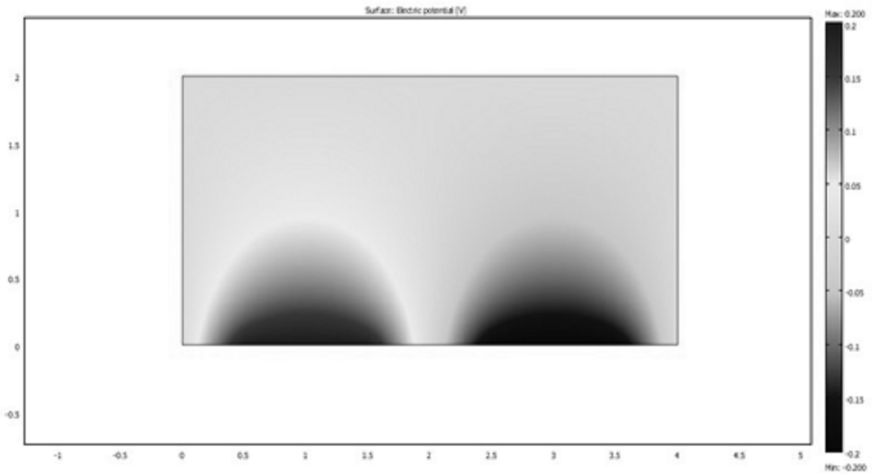

Figure 3.5 – (a)Plot showing the finite element solution for the electric potential obtained from a numerical solution of the governing Laplace equation in the model geometry. The model geometry consists of two adjacent electrodes with 180 degree phase shifted potential applied to them. The applied amplitude is 10 volts. All the lengths have been normalized with respect to the electrode width(W).

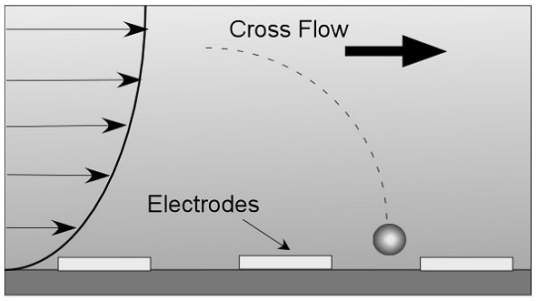

(a)

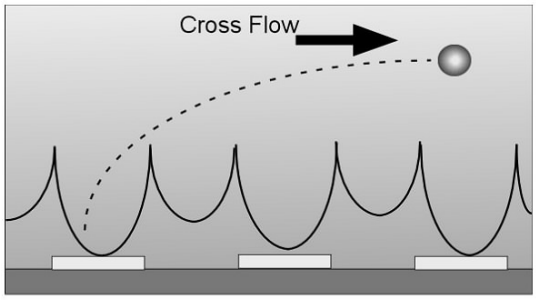

(b)

Figure 3.6 – Schematic showing a conceptual representation of the particle trajectory in the rectangular channel geometry. (a) The particle is deposited on the surface in presence of the cross flow. (b) The particle is carried away from the surface under a combination of repulsive DEP force and the ensuing cross flow in the system thus preventing further deposition.

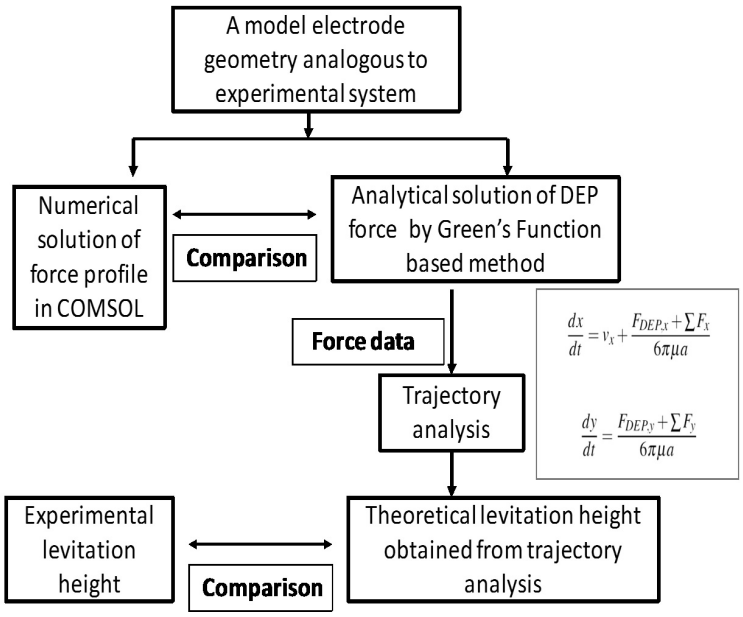

Figure 3.7 – Schematic showing the numerical methodology adopted for the solution of particle trajectory and their comparison with experimental results.

Chapter 4

Experimental Observation

4.1 Experimental Setup

The experimental setup consists of a function generator (Tektronix, AFG320), amplifier (FLC, F20AD) and an oscilloscope (Tektronix, TDS2002) in order to quantify the input and output waveforms. The electrical connector wires were metal bonded to the bonding pads of the DEP chip using conductive epoxy to ensure proper connectivity.

Figure 4.3(b) depicts a schematic of the experimental setup. The electrodes were subjected to an AC sinusoidal input at 180 degrees phase shift and the observations were made at different voltages and frequencies. The flow cell was mounted on the motorized stage of a microscope (Carl Zeiss, Axiovert 200M) and the microscope objective was focussed on the electrode plane. Image acquisition was done using a digital camera (Basler 102FC) and with an image acquisition software (NI Vision 8.0, National Instruments). Two 10 ml syringes were used with a syringe pump (New Era Pump Systems Inc, NE-1000) to inject and withdraw the aqueous colloidal suspension in the rectangular flow channel [Molla, 2004].

4.1.1 Crossflow Channel

A schematic of the flow cell along with it's components is shown in Figure 4.3(a). The chip was housed inside an aluminum holder with a PDMS spacer inserted between the cover glass plate and the chip thus sealing the rectangular flow channel.

4.1.2 Particle Suspensions

The particles used as model foulants were, white polystyrene sulfate latex (mean diameter 2.0 ± 0.1 μm and 5.0 ± 0.20 μm) (IDC Corp, USA), silica (Polysciences, USA) (mean diameter 2.0 ± 0.1 μm and 5.0 ± 0.20 μm) and amidine polystyrene (IDC Corp, USA) (mean diameter 2.0 ± 0.1 μm) respectively . The original stock solution (10^{10} particles/ml) was sufficiently diluted with deionized water (Millipore, USA) to prepare 100 ml suspension, having a resulting concentration of 2.1×10^6 particles/ml. The pH and conductivity of the suspension were maintained as 7.1 and 4 $\mu S/cm$ and measured with dual conductivity meter (Accumet AR50). Prior to the experiments, the particle charges were verified by measuring their zeta potential in separate suspensions using a zeta potential analyzer, the Zetapals(Brook Haven Instruments). Other properties of the colloidal suspension used are outlined in Table A.1.

4.2 Electrode Array Fabrication

4.2.1 Mask Preparation

A design of the interdigitated electrode array was made using L-Edit (Tanner Research Inc.) design software. The electrode design was transferred to a chrome mask with the aid of a pattern generator (Heidelberg model DWL 200) [Molla, 2004]. The mask was inspected thoroughly under a microscope objective, to ensure absence of extraneous particles on the mass surface that may pose problems for the lithography steps. A design of the mask done in L-edit has been shown in Figure 4.1.

4.2.2 Photolithography

Experiments were carried out with a planar microelectrode interdigitated array, fabricated on a glass substrate using standard photolithography techniques. The electrode array was fabricated with an electrode width (W) of 50 μm and the gaps (G) between the consecutive electrodes set between 25 to 50 μm. The schematic containing the electrode array dimensions is described in Figure 3.1(b). The electrode array consists of 200 interdigitated electrodes. The thickness of the gold layer is approximately 300 nm over a 25 nm thin chrome layer initially deposited on the glass substrate [Molla, 2004]. A comparison of the two electrode configurations indicate that the latter design has

better yield in terms of fabrication. The asymmetrical design of electrodes was chosen in order to explore the effect of the asymmetry of electrode geometry in the levitation. However, the 50 μm $\times$ 50 μm design was found to be the best in terms of fabrication as the problem of shorting of the adjacent electrodes was found to be minimum in this case. A schematic of the numerous steps involved in the fabrication process have been outlined in Figure 4.2.

The electrode design was transferred to a chrome mask with the aid of a pattern generator (Heidelberg model DWL 200). In the next step, the mask pattern was embedded on a borofloat glass substrate by optical lithography. The photoresist (HPR-504) was spin coated on the substrate followed by subsequent baking at 150 degree Centigrade. The substrate was aligned using a suitable mask aligner and exposed to UV light of wavelength 350 nm. The exposed photoresist was then developed using the Microposit 354 developer solution [Molla, 2004]. After developing the resist, the substrate was subsequently metal etched and diced to the required chip dimensions [Molla and Bhattacharjee, 2007]. The resultant glass chip dimensions were 50mm in length and 25 mm in width, respectively, with an average thickness of 2.5 mm.

A successful fabrication process largely depends on the proper mask design and diligent adherence to cleanroom protocols. Proper execution of the steps outlined in the cleanroom are of utmost importance while fabricating the electrode array. Some salient points while performing fabrication are outlined as follows.

1. After printing the mask, it is properly inspected under a microscope. Any particles entrained on the mask can cause a defective feature in the photolithography steps. Thus it is imperative to inspect the mask closely for early defects before the feature is transferred to the substrate.

2. The exposure time in the lithography station is increased to six seconds. Higher exposure time leads to better aspect ratios as the photoresist is fully cured by the UV light. A slight overexposure might actually prove beneficial to the process depending on the intricacy of the feature size.

3. In the metal etching step, the visible color change serves as an indication of the chrome etch. Failure to remove the substrate promptly leads to frequent overetching, thus causing the underlying chrome layer to

be removed from sporadic locations in the electrode array. This can contribute to severe issues like flaking of the gold electrodes.

4.3 Experimental Procedure

Prior to the experiments, the suspension of particles was sonicated in a water bath at 25 degree Centigrade to ensure uniformity of particle size and prevent flocculation of the particles. A 10 ml sample of the suspension was taken in the syringe and pumped through the inlet to maintain a steady cross flow of 10 ml/hr. A withdrawal syringe connected to the outlet was operated at the same rate to withdraw fluid from the chamber. The intermediate spacer has a thickness of 1 mm. The channel dimensions are $10mm \times 20mm \times 1mm$ respectively. Based on the above channel dimensions and corresponding flow rate, the average cross flow velocities are calculated.

Initially, a 10X microscope objective was focussed on the electrode plane in the absence of any applied potential. When the particles on the electrode plane levitated on applying a potential, the objective was refocussed on the plane of the levitated particles. The resultant particle levitation height is obtained as a difference in height between the initial and final focussed positions as obtained from the microscope readings. Three separate experimental runs were conducted for each value of applied voltage. The levitation data is therefore based on the method of ensemble average of the three readings, rather than individual particle tracking method typically resulting from a Micro-PIV approach [Molla, 2004]. The same procedure was repeated to get the levitation height data for different particle sizes and cross flow velocities. A second set of experiments were done to study the effect of frequency in the multi-component suspension. The experimental method to measure the levitation height is outlined in the Figure 4.4.

The measurement of a stable levitation height proved to be considerably difficult in a cross flow system because of the lateral movement of the levitated particles along the electrode plane. The tangential flow causes the particles to be dislodged from their maximum levitated positions i.e. the DEP force peaks as shown in Figure 5.9, to the gaps where the force decreases exponentially [Molla, 2004]. In order to minimize this variation, an arithmetic mean of three

levitation heights were taken at the same location for each reading. In addition to this, the readings were taken from different regions of the given electrode geometry.

4.4 Observations

This section explains observed effects of colloidal silica particle in the experimental system when an electric field is applied to the electrodes. Figure 4.5(a) shows the initial instant as the silica particles (mean diameter $5\mu m$) are deposited on the surface of the glass substrate. When the AC signal is applied at a frequency of 1 MHz, the silica particles on the surface of the electrode is acted upon by negative DEP force. Figure 4.5(b) shows the particles as they move away from the electrode edges toward a region of lower electric field. In Figure 4.5(c), the silica particles are levitated from the channel surface by the effect of negative DEP and are carried away by the cross flow.

An interesting future work in relation to DEP can be the use of the concept of microfluidic scavenging in biofouling prevention. Since the DEP force is directly proportional to the particle volume, the larger particles are typically removed with ease rather than the smaller ones. This has relevance especially in preventing biofouling in channels.

In the above context, a negatively charged foulant sits on the channel surface suitably embedded with an interdigitated electrode array by microfabrication techniques as shown in Figure 4.6 (a). The size of the foulant is small enough so that the dielectrophoretic force acting upon it is not significant and cannot levitate the foulant on it's own. When a cross flow with a larger positively charged particle is introduced in the chamber, these larger particles will adhere to the smaller negative foulants and form doublets thereby increasing the effective size of the original species. Since the dielectrophoretic force is a function of the particle size, the doublet will experience an enhanced repulsive dielectrophoretic force and will be removed from the channel surface. The combined doublets can then be collected at the outlet and upon adjustment of the pH of the solution, the original particles would be recovered at an isoelectric pH. This novel technique has potentially viable applications in the prevention of biofoulants adhering to the surface of microfluidic channels.

4.5 Summary

A detailed set of experimental observations in a parallel electrode array was presented in this chapter. The experimental setup and the procedure has been described in detail along with the parameters used for the associated numerical simulations. Further, the intricacies of fabrication process and the optimum parameters to be used in fabrication have been separately outlined. The chapter also presents the major impediments faced in terms of device fabrication and the importance of proper cleanroom protocols to assure defect free devices. The experimental observations display negative DEP in silica particles at a frequency of 1 MHz. This experiment demonstrated that DEP is capable of levitating 5 μm sized particle from a fouled surface and thereby can prevent further fouling of surfaces. The observations further indicate that DEP in combination with a cross flow is an effective means of preventing particle deposition at the initial fouling stages. In addition to DEP, the particles have been observed to form long chains when subjected to the AC field. This suggests that although a system of non interacting particles has been assumed for simplicity, particle interactions may play a significant role in determining the behavior of the experimental system which can be an interesting direction for future work. The above experimental observations provide the background for investigating the behavior of the individual components like silica and polystyrene in a binary system which is explored in the next section.

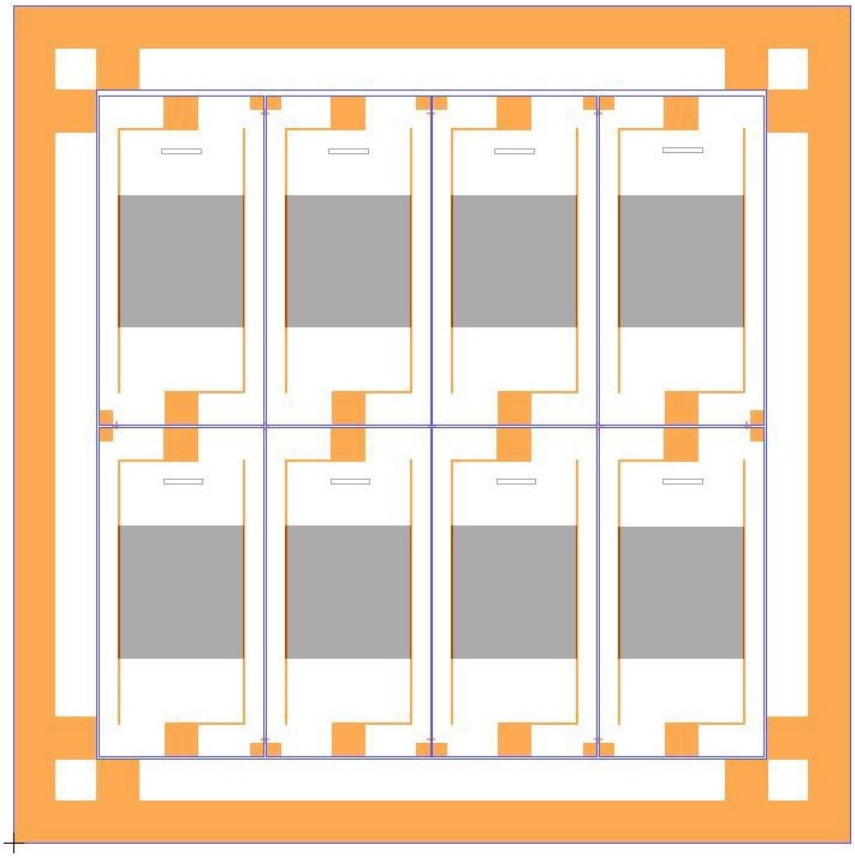

Figure 4.1 – Schematic showing an L-edit drawing of the mask pattern. The orange color indicates the chrome layer constituting the mask and the UV light can travel through the transparent portions.

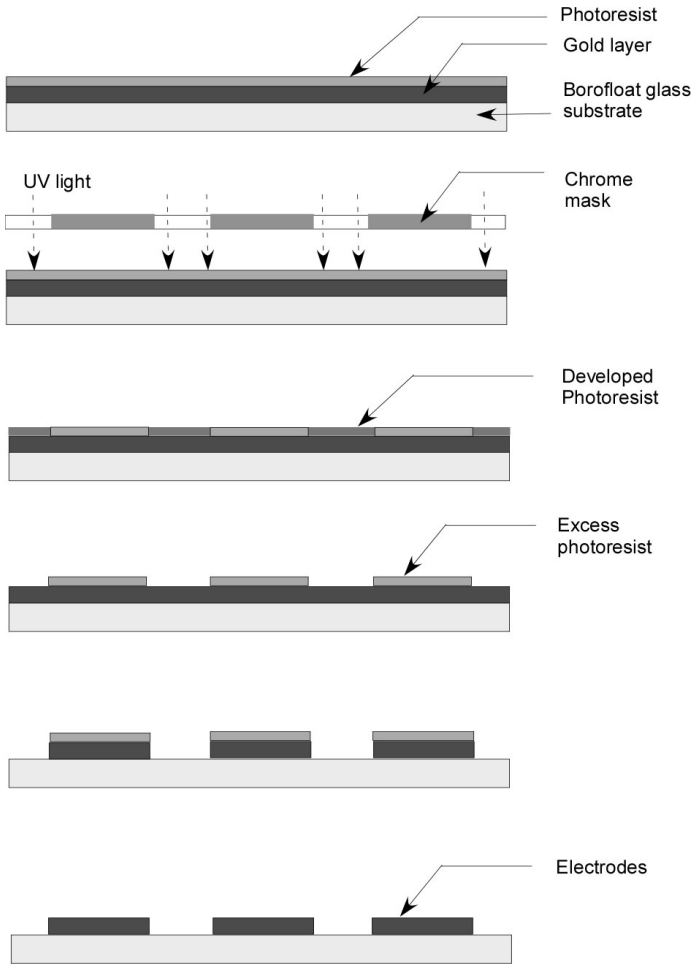

Figure 4.2 – Schematic showing the different steps in the fabrication process of the dielectrophoretic chip.

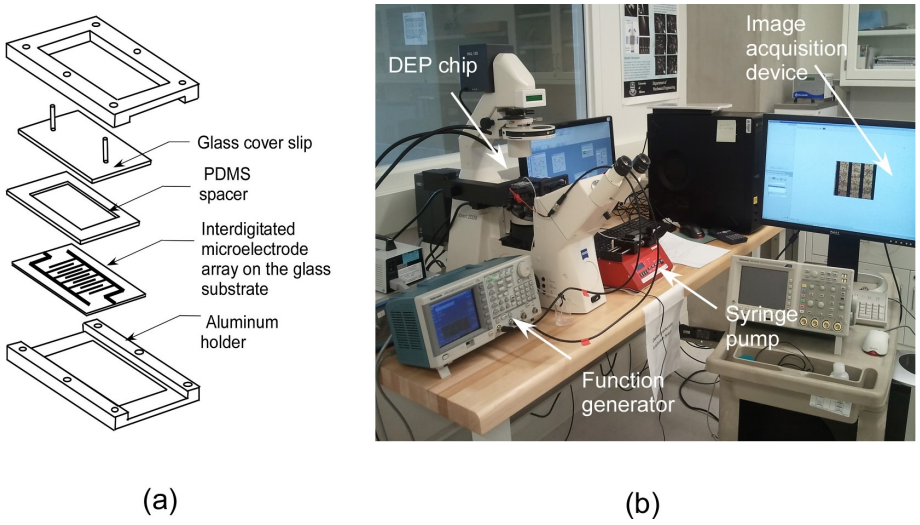

Figure 4.3 – Schematic showing the (a) flow cell components, (b) the experimental setup. The DEP chip in the setup is actuated by 180 degree phase shifted AC signals while a syringe pump circulates the colloidal suspension through the flow cell.

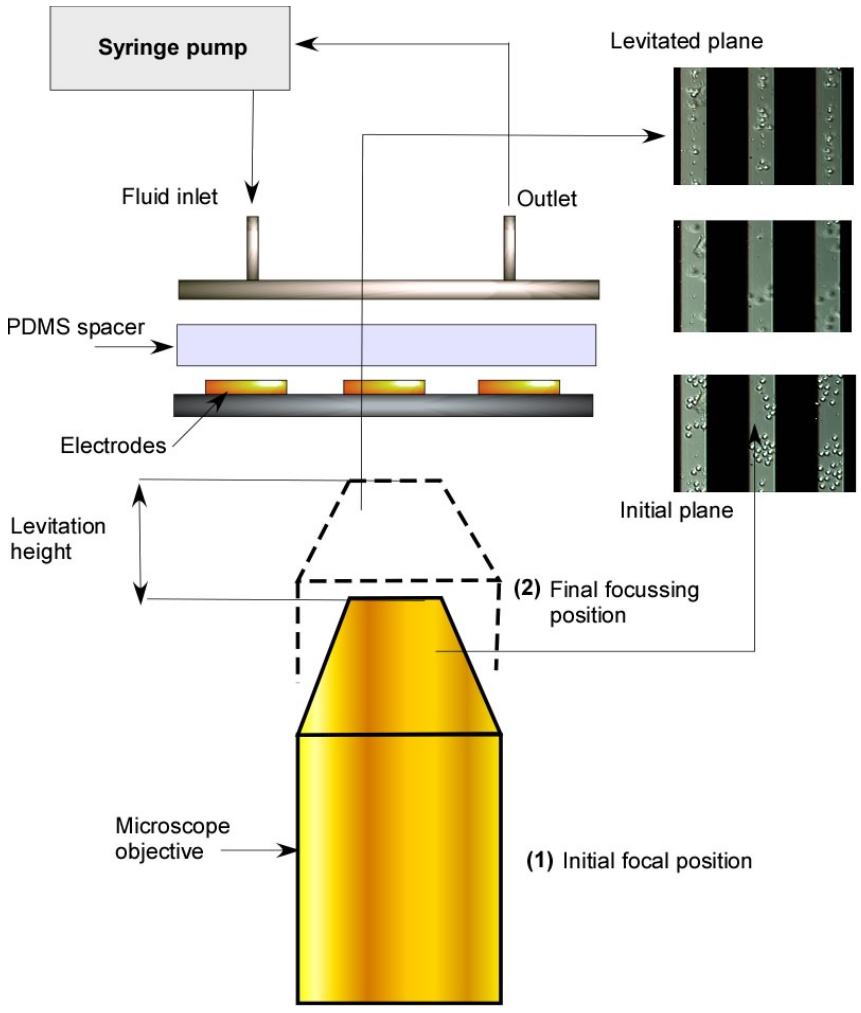

Figure 4.4 – Schematic showing the experimental method for determining the experimental levitation height. The syringe pump circulates the colloidal suspension in the rectangular chamber. Initially, the microscope objective is focussed on the particles settling on the electrode surface and this defines the initial position. With the application of voltage the particles levitate to a different plane and the objective is refocussed on the levitated position as seen from the image. The levitation height is obtained from a difference between the initial and final focal positions of the objective.

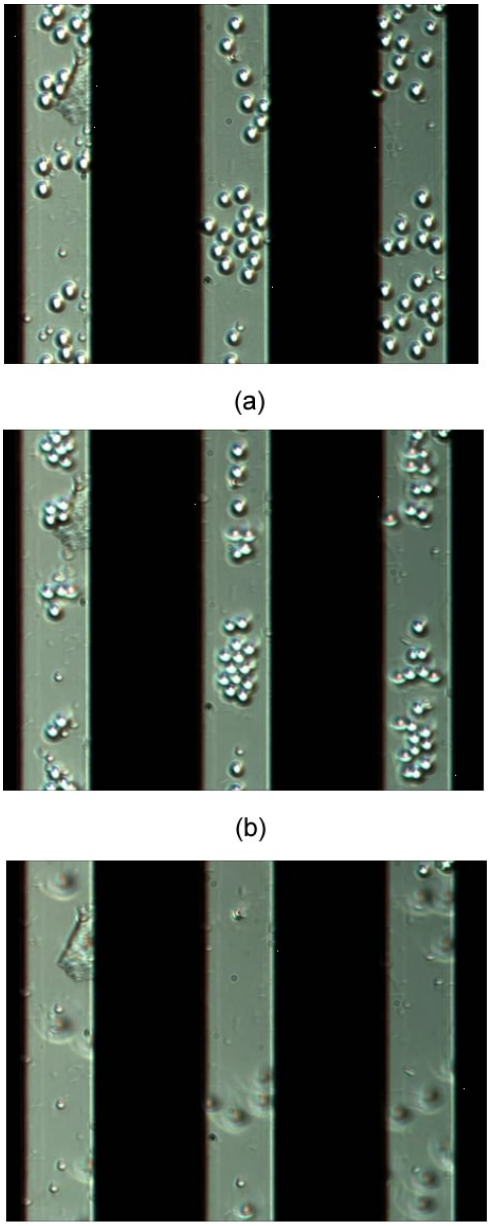

Figure 4.5 – Video images showing negative dielectrophoresis in silica at 1 MHz. (a) At the initial instant the silica particles are deposited on the electrode surface.(b) On applying a 180 degree phase shifted potential the particles move away from the electrode edges due to negative DEP. (c) The silica particles are carried away by the cross flow thereby preventing further deposition. The cross flow velocity is 1.4×10^{-6} m/s. The electrodes have width and gap of $50\mu m$ and $25\mu m$ respectively.

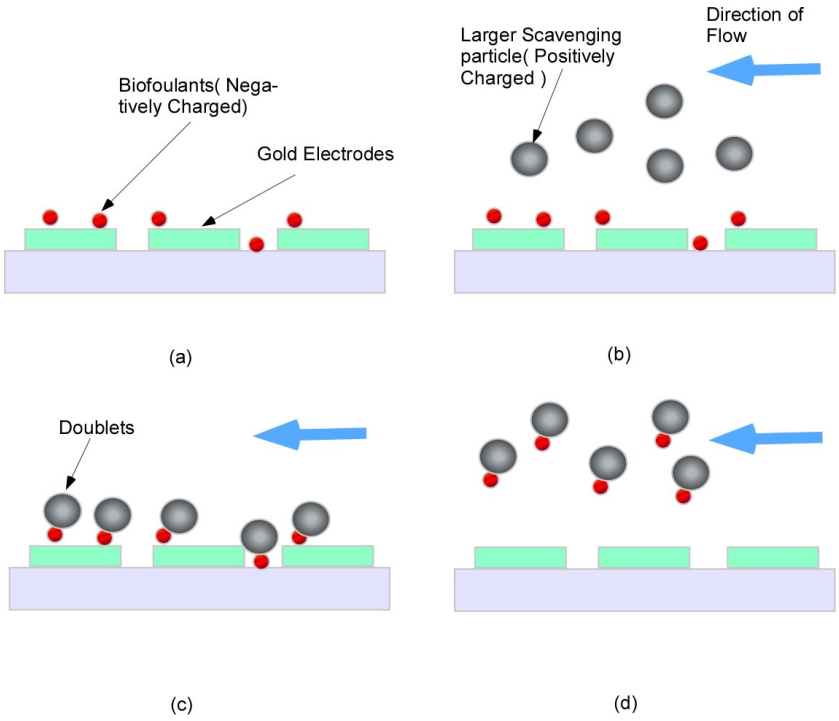

Figure 4.6 – Schematic showing the effect of biofouling and it's subsequent removal by the attachment of bigger scavenging particles to the smaller foulant species.

Chapter 5

Results and Discussion

5.1 Dielectrophoretic Levitation in Single Component Suspension

The experimental results on particle levitation are discussed by comparison of a series of snapshots taken on a fixed region of the interdigitated electrode array at a regular interval of 0.5 seconds. Figure 5.1 depicts five images taken over a representative section of the electrode array.

With a constant cross flow velocity but in absence of any applied voltage (Figure 5.1(a)), the particles deposit on the electrode surface. On actuation of the electrode array by a 180 degree phase shifted AC potential of 10 volts peak to peak and frequency of 1 MHz, the particles residing on the interdigitated electrodes experience negative DEP. Consequently, these particles move away from the electrode edges towards regions of lower field gradient as shown in Figure 5.1(b). After a period of 1 second, the particles on the electrodes become blurred as they continue to move away from the focal plane of the microscope objective. The particles are lifted off from the electrode plane and subsequently carried away by the cross flow (Figure 5.1(c)). The electric field is then switched off, which initializes the onset of particle deposition on the surface due to the absence of any dielectrophoretic force as demonstrated in Figure 5.1(d). The complete deposition is evident from Figure 5.1(e). This interprets that deposition is strongly influenced by gravity even in the presence of a cross flow in the system.

5.1.1 Effect of Voltage

Figure 5.2a and b depict the variation of levitation height with applied voltage in a single component suspension. The cross flow velocity in the flow cell was maintained at 1.4×10^{-6} m/s. The amplitude of the AC signal ranges from 1 to 10 V and the applied frequency is 1 MHz. From calculations of the Clausius Mossotti factor for silica and polystyrene in water, it is expected that both the particles will exhibit negative DEP effect at 1 MHz. It is evident from Figure 5.2(a) that, an amplitude of 10 V can cause a levitation of 70 μm in the 5 μm sized silica particle in the flow cell. At the same amplitude, it is observed from Figure 5.2(b) that, polystyrene sulfate particles attain a levitation height of 100 μm due to its low material density when compared to silica. No distinguishable levitation height was observed in silica particle corresponding to the amplitude of 1 and 2 volts, since the electrical force was not sufficient to overcome the weight of the heavier silica.

5.1.2 Effect of Variation of Cross Flow Velocity

Figure 5.2 also demostrates the variation of particle levitation height for two different cross flow velocities (1.4×10^{-6} m/s and 4.2×10^{-6} m/s) in the channel. As discussed before, the average cross flow velocities ($\mathbf{v_x}$) were calculated based on the channel area and respective flow rates of 10 ml/hr and 30 ml/hr. The above velocities assure a fully developed flow for our experimental design. An increase in $\mathbf{v_x}$ results into corresponding increase of $\mathbf{u}$ as evident from Equation 3.34. Therefore, the particles undergo dominant convective transport in axial direction with increased axial velocity ($\mathbf{u}$), as compared to their transverse motion under repulsive DEP. As a result, the particles show lesser levitation height in the observed region of the electrode geometry.

5.1.3 Effect of Particle Size

A comparison of the levitation heights of 2 μm and 5 μm sized silica and polystyrene sulfate particles under a cross flow velocity of 1.4×10^{-6} m/s is shown in Figure 5.3(a) and (b). The 5 μm silica particles show a higher value of levitation than the 2 μm particles. Larger particle radius translates to a higher degree of DEP force (Equation 3.9), but in turn also corresponds to simultaneous increase in gravity force due to the enlarged particle volume (Equation 3.38). Both DEP and gravity forces are dependent on particle volume or cube

of radius, whereas drag is proportional to particle radius. From Equation 3.39b it is clear that, the migration velocity is proportional to the square of particle radius. Therefore, a larger particle would attain a higher migration velocity than the 2 μm particle. This involves a net increase in the value of the transverse component ($\mathbf{v}$ in Equation 3.35) of the migration velocity for the larger particle, since the axial velocity component ($\mathbf{u}$ in Equation 3.34) stays the same for both particle sizes. The larger particles thus experience higher levitation heights due to increased $\mathbf{v}$. When compared between the silica and polystyrene particles in Figure 5.3(a) and (b), the silica particles show a lower levitation height for the same particle size on account of it's higher density.

5.1.4 Effect of Surface Charge

In this section, the levitation heights of oppositely charged 2 μm amidine terminated polystyrene and 2 μm polystyrene sulfate particles are compared. At neutral pH, the amidine and sulfate terminated polystyrene exhibited zeta potential values of +25 mV and -30 mV respectively.

It can be observed from Figure 5.4 that, the particle charge has negligible effect on dielectrophoretic levitation. The complex permittivity of the dielectric particle suspended in the medium is given as Morgan and Green [2003] :

$$\epsilon_p{}^* = \epsilon_p - i\frac{\sigma_p}{\omega} \tag{5.1}$$

where ϵ_p^* and ϵ_p are the complex and absolute permittivities of the particle, while σ_p and ω stand for the particle conductivity and applied frequency respectively.

From Equation 5.1, it is apparent that the complex permittivity is dependent on the applied frequency. A calculation of the Clausius-Mossotti factor for the two species comes out to be the same negative value, e.g. -0.47 at 1 MHz. This manifests that two particles sharing identical particle radius and real part of Clausius-Mossotti factor will experience similar DEP force. As a result, both the particles show almost identical levitation heights as depicted in Figure 5.4.

5.2 DEP with Binary Colloid Suspension

5.2.1 Levitation Height Measurement in Binary Suspension

In this section, the levitation heights obtained for individual species in a binary suspension of silica and polystyrene particles are analyzed to determine the effectiveness of repulsive DEP forces in levitating the colloidal particles from a planar substrate.

Figure 5.5 shows a comparison between the levitation heights of similar sized (5 μm) silica and polystyrene particles in a binary suspension with an applied cross flow velocity of 1.4×10^{-6} m/s. Considerable differences can be observed in the smaller amplitude range of 1 - 2 V at 1 MHz, where the silica did not show any appreciable movement, while the polystyrene particles were levitated to an average height of 48 μm. On increasing the voltage further, both the silica and polystyrene particles were found to levitate to different planes which are clearly distinguishable under the microscope objective.

Figure 5.6 shows the variation of levitation height with the applied voltage for a binary suspension consisting of 2 μm polystyrene sulfate and 5 μm silica particles. It can be seen from the figure that, the levitation of the individual particles is not much influenced by the coexistence of the other component and the values closely resemble the observed levitation in single component suspensions. The 5 μm polystyrene exhibits a maximum levitation of 100 μm whence the 2 μm silica corresponds to a levitation of 50 μm for the same applied amplitude of 10 V and an applied frequency of 1 MHz.

Figure 5.7 shows a comparison between the levitation of 5 μm polystyrene and 2 μm silica particles under a cross flow. It can be observed from the figure that, the polystyrene particle attains a levitation height of 90 μm while the 5 μm silica shows a levitation height of 72 μm for an applied voltage of 10 V.

5.2.2 Selective Levitation from a Binary Mixture

The separation of particles by selective levitation of a particular component in a binary mixture offers diverse potential applications. Figure 5.8(a) depicts

the initial condition before application of voltage. Figure 5.8(b) shows that, when the electrodes are actuated by voltage of 4 V at a frequency of 10 kHz, the polystyrene particles undergo positive DEP and are attracted towards the electrode edges. In contrast, the silica particles experience negative DEP at this frequency and as a result, are repelled to the electrode gap regions. On further increasing the applied voltage to 10 V keeping the frequency fixed, the heavier silica particles levitate from the surface and are removed by the cross flow in the system as demonstrated in Figure 5.8(c). Silica is generally more susceptible to foul the surface due to its higher density than polystyrene. Our experiments demonstrate the removal of a more potent fouling species in a multi-component fouling scenario. As observed earlier, the polystyrene particles can also be levitated by increasing the applied frequency to 1 MHz.

5.3 Numerical Levitation Height and Validation with Experiments for Single Component Suspension

5.3.1 Analytical and Numerical Electric Field and Force Comparison

Following the analytical and numerical approach outlined in the previous sections, the electric field and force profiles are obtained from the solution of Equations 3.32a - 3.32e and Equation 3.9 respectively.

Figure 5.9(a) shows the analytical and numerical values of the scaled norm of the electric field for the considered electrode geometry. The magnitude of norm of the electric field is given as $E = \sqrt{E_x^2 + E_y^2}$, where E_x and E_y are the corresponding electric field components along the horizontal and transverse directions. The maximum value of the electric field is observed to be in the order of 10^6 V/m. As evident from the figure, the numerical solution exactly conforms to the analytical result. However, the analytical peak values are found to be slightly higher than the numerical values. The electric field profile display sharp peaks at the electrode edges due to the higher values of electric field gradient at the edge of the electrodes.

Figure 5.9(b) illustrates a typical DEP force profile on a representative

section of the considered electrode geometry. The figure also shows that, the repulsive DEP force has a large spike near the electrode edge. This force is significantly different at the middle of the electrodes than the gap region which displays a higher force value. The negative sign of the force denotes the repulsive nature of the above DEP force field. The parameters of the simulation are characteristic of a polystyrene in water system at high frequency as depicted in Table A.1. The analytical force values calculated here are employed in the trajectory model for obtaining the theoretical levitation height of a particle.

5.3.2 Numerical Prediction of Levitation Height of Single Particle from Trajectory Results

The levitation heights for a single particle are obtained from the numerical solution of Equations 3.34 and 3.35. Figure 5.10 shows the corresponding levitation heights for polystyrene and silica particle over a fixed electrode region for three representative amplitude values. The system cross flow velocity is 1.4×10^{-6} m/s. Figure 5.10(a) shows the trajectories of a single 5 μm polystyrene sulfate particle for an applied voltage range of 3-10 V and a frequency of 1 MHz. Under similar conditions the trajectory of a single silica particle is also depicted in Figure 5.10(b). Both the graphs show that, the particle follows a higher trajectory on increasing the applied potential as the dielectrophoretic force increases with enhanced electric field gradients. Also, the silica being a heavier particle assumes a steady state levitation height much faster than polystyrene sulfate particles for the same value of applied potential and hence displays lesser levitation heights.

5.3.3 Numerical and Experimental Levitation Heights

Figure 5.11(a) and (b) show the comparison between the numerical results and experimental observations for polystyrene and silica particles respectively. The numerical model successfully captures the levitation trend. The discrepancies in the numerical and experimental levitation results for a single particle can be ascribed to the assumptions made for simplifying the formulation of the mathematical model. In this model, the dielectrophoretic force is considered independent of any multipolar or multi-body effects. The physical properties used for the model predictions were taken from literature which can further contribute to the deviation between experimental and numerical results.

5.4 Summary

This chapter mainly comprises of the numerical and experimental results along with the relevant discussions. The numerical results for the electric field and force was compared with the analytic solutions obtained from the Green's theorem approach. In addition, the trajectory analysis results obtained from the previously described numerical model was compared with the experimental data. The trajectory analysis data show reasonable agreement with the observed experimental levitation height. Moreover, the effects of dielectrophoresis on individual components was analyzed in a binary suspension. The results suggest that DEP can engender selective particle levitation when applied to a multi component system and provides an effective method to alleviate fouling in a selective manner by variation of process parameters. In the next section, the treatise will be concluded highlighting the conclusion and future scope of research obtained from analysis of results presented in this chapter.

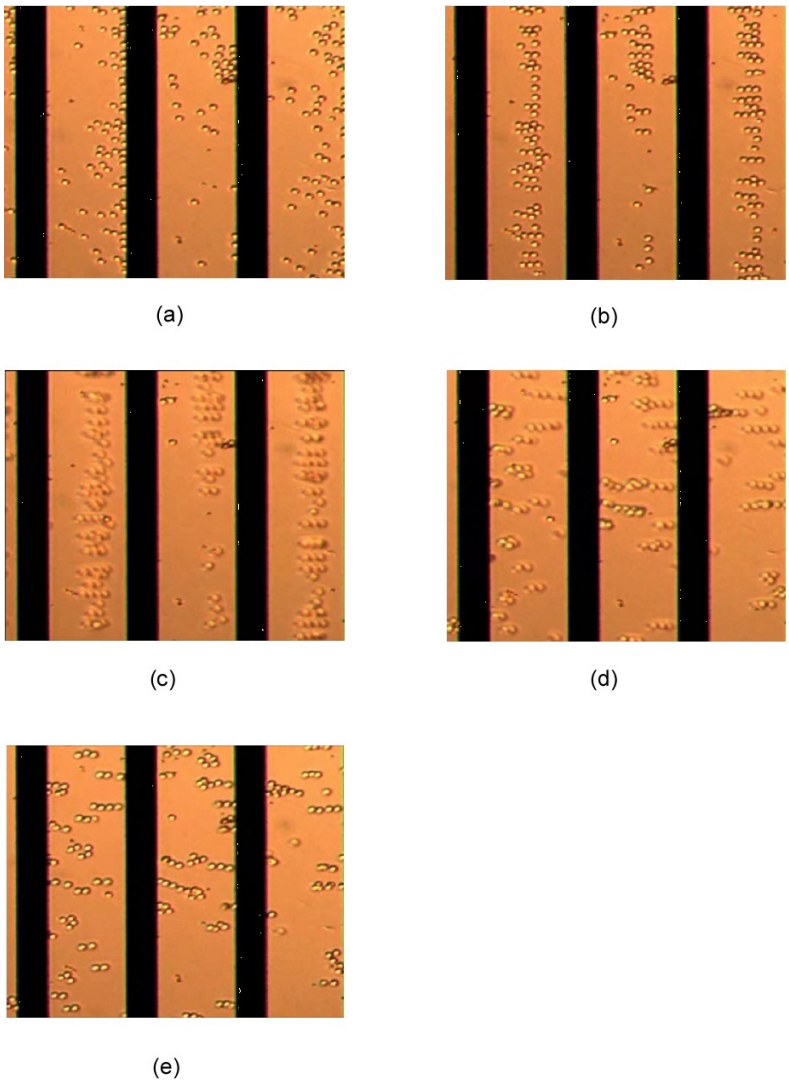

Figure 5.1 – Video images of silica particles inside the cross flow channel taken at intervals of 0.5 seconds. (a) At the initial instant t=0, the particles are uniformly distributed across the electrode surface.(b) At t=0.5 seconds the particles are subjected to negative DEP force thereby migrating towards the lower electric field region. (c) At t=1 second the particles particles are appearing blurred as a result of the levitation and carried away by the flow. (d) The electric field is switched off and the particles begin to deposit anew on the electrodes.(e) The particles completely deposit on the electrodes even in presence of the cross flow velocity.

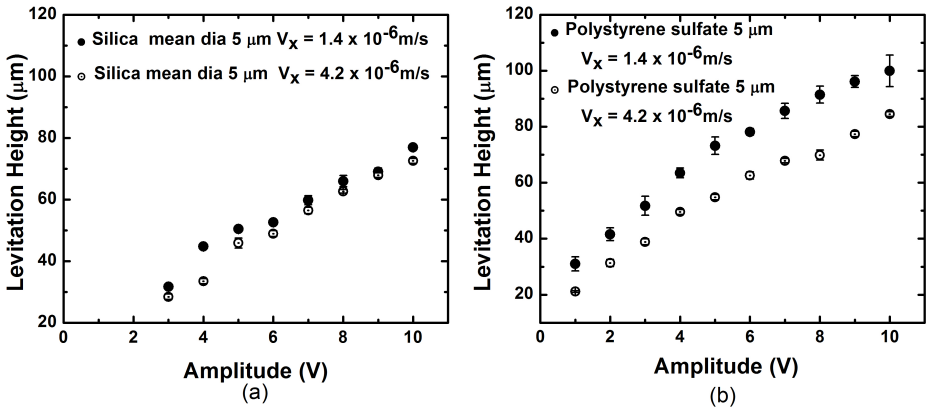

Figure 5.2 – (a) Plot showing the effect of applied amplitude and cross flow in a single component system consisting of 5 μm silica particles and (b) 5 μm polystyrene sulfate particles with two different cross flow velocities

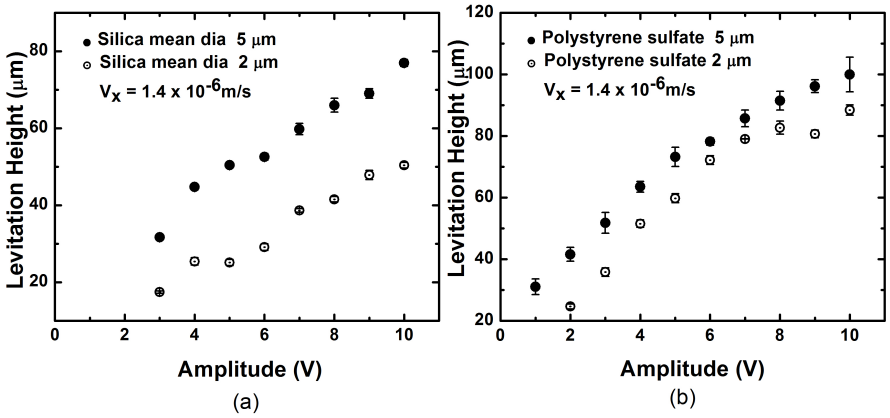

Figure 5.3 – (a) Plot showing a comparison of the levitation heights for different sizes of silica particle, namely 5 μm and 2 μm in presence of a cross flow (b) The same is shown in the case of polystyrene sulfate particles measuring 5 μm and 2 μm. The applied cross flow velocity is 1.4×10^{-6} m/s.

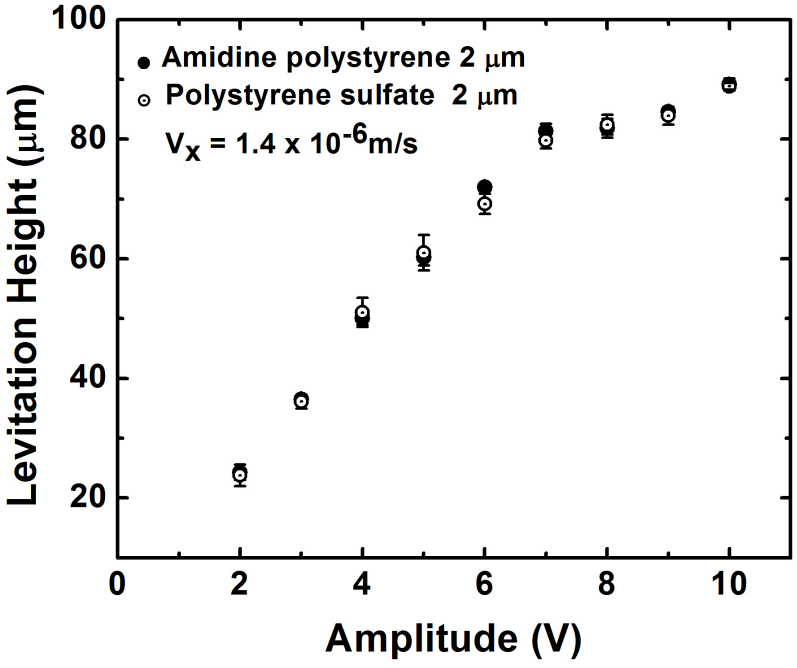

Figure 5.4 – Figure showing the comparison between the levitation height of 2 μm amidine and 2 μm polystyrene sulfate particles. The applied cross flow velocity is 1.4×10^{-6} m/s.

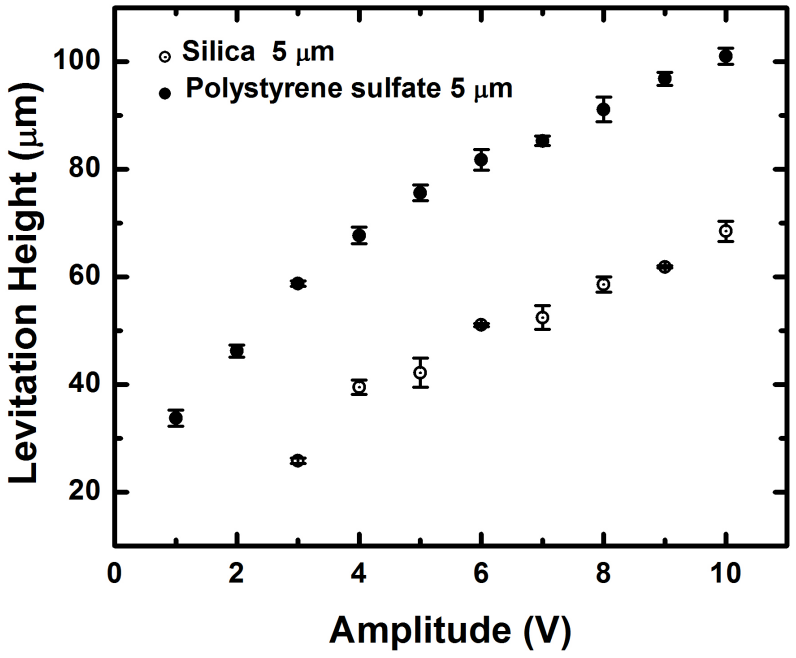

Figure 5.5 – Plot showing a comparison of the levitation heights of silica and polystyrene in a binary suspension under a cross flow rate of 10ml/hr for 5 μm silica and 5 μm polystyrene. The applied cross flow velocity is 1.4×10^{-6} m/s.

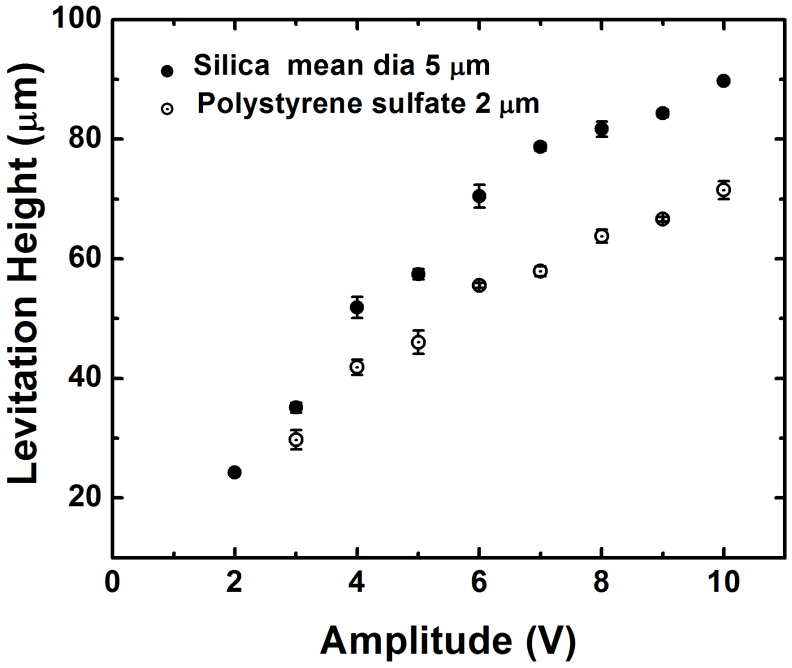

Figure 5.6 – Plot showing a comparison of the levitation heights of silica and polystyrene in a binary suspension under a cross flow rate of 10ml/hr for 5 μm silica and 2 μm polystyrene. The applied cross flow velocity is 1.4×10^{-6} m/s.

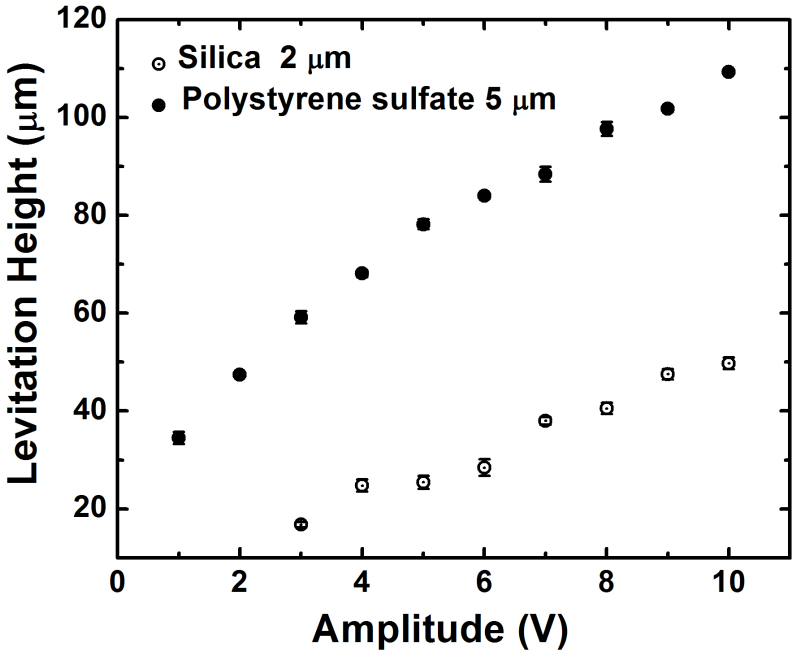

Figure 5.7 – Plot showing a comparison of the levitation heights of silica and polystyrene in a binary suspension under a cross flow rate of 10ml/hr for 5 μm silica and 2 μm polystyrene. The applied cross flow velocity is 1.4×10^{-6} m/s.

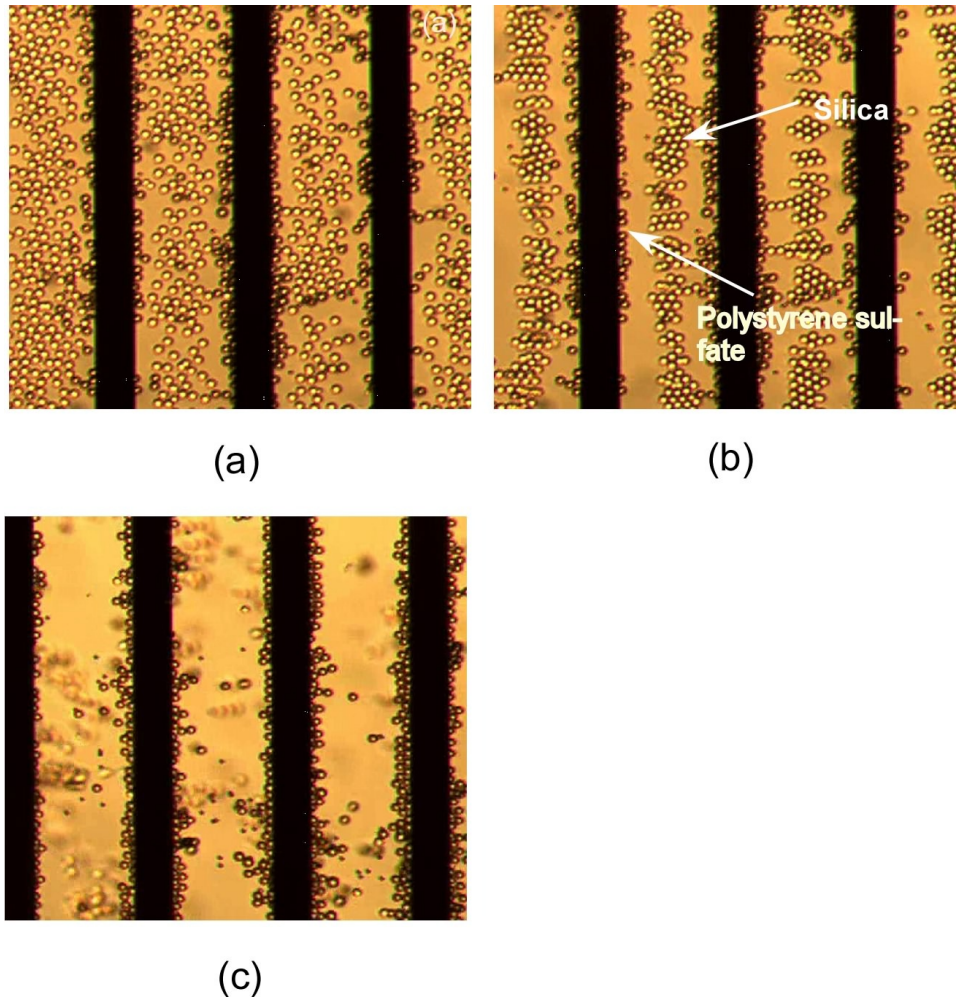

Figure 5.8 – Figure showing the separation of 5 μm mean diameter silica and polystyrene in a binary suspension at an applied frequency of 10 kHz. The width of the electrodes in the above plot is 25 μm while the electrode gap is 50 μm (a) Initial condition before application of potential (b) A 4V potential is applied which causes the silica to be repelled from the electrode edges while polystyrene is attracted to the edges. (c) At 10 V, the cross flow carries away the heavier silica thereby trapping the polystyrene on the electrode surface. The applied cross flow velocity is 1.4×10^{-6} m/s.

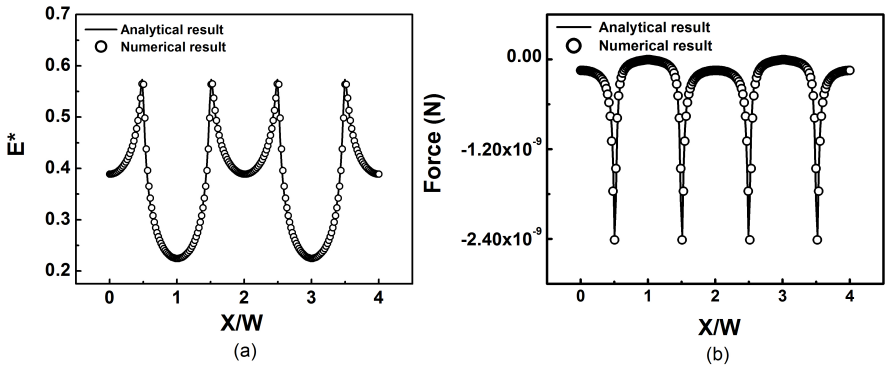

Figure 5.9 – (a) Plot showing the variation of the scaled electric field (E^*), along the horizontal direction. The vertical axis represents the scaled electric field. The actual value of the field is given in V/m by multiplying the plot values by a magnitude of 10^6, whereas the X-axis represents the non dimensional distance along the electrode array scaled with respect to electrode width . Both the width and the gap of the electrodes have been set as 50 μm (b) Plot showing the negative DEP force(N) on the electrode geometry of width and gap 50 μm respectively.

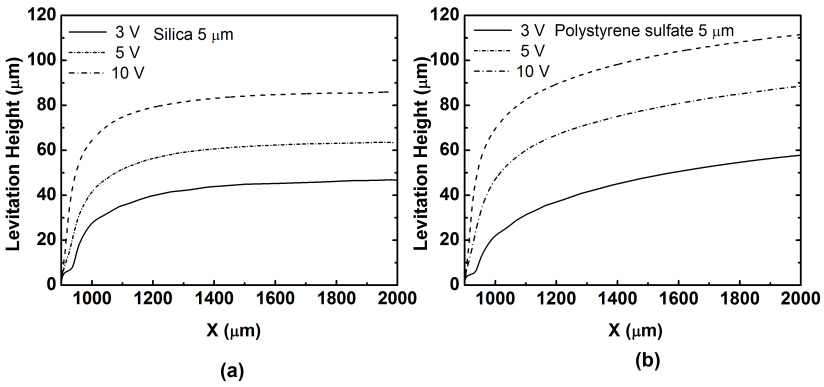

Figure 5.10 – Plot showing the particle trajectory of (a) 5 μm silica (b) 5 μm polystyrene sulfate at a frequency of 1 Mhz and a voltage range of 3-10 V. The particles are released from the same position on the electrode. The X and Y axes represent the axial and transverse distances in μm for the considered system geometry .

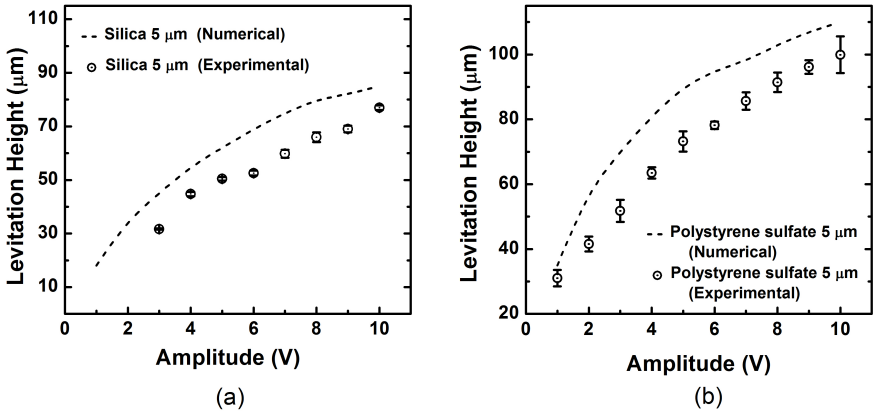

Figure 5.11 – Figure showing the comparison between experimental levitation results and trajectory analysis for (a) 5 μm silica (b) 5 μm polystyrene at a frequency of 1 MHz and a voltage range of 1-10 V.

Chapter 6

Conclusions and Future Work

6.1 Conclusions

In this study, AC dielectrophoresis has been demonstrated as a viable method for fouling prevention in a multi-component colloidal system. It has been shown through experiments and a simple trajectory analysis that, AC dielectrophoresis can provide an efficient means of preventing colloidal deposition on channel walls irrespective of type of charge of the fouling species. The following key conclusions can be drawn from the presented work.

1. The experiments clearly demonstrate the efficacy of negative DEP as a method for selective particle levitation in a multi-component system. The results indicate that negative DEP can lift the foulant microparticles more than 10 μm under a suitably applied voltage and frequency [Molla, 2004], thereby effectively preventing deposition on the channel wall.

2. The levitation of specific colloid components can be achieved by selectively tuning the frequency of the applied AC field. This provides considerable flexibility regarding fouling management by preventing the adsorption of a more deleterious foulant from a mixture.

3. The numerical simulations indicate that a simple force balance is adequate in capturing the dominant particle levitation effects quite accurately. The extent of levitation is considerable compared to most other known repulsive colloidal force based techniques.

6.2 Future Work

1. The theoretical model developed in the present work focuses only on dielectrophoretic force. However, other factors influencing the particle motion like electrothermal flow, and multipolar effects due to the presence of higher order poles have been neglected for simplicity. Including the above terms will sufficiently enrich the model and lead to a more realistic comparison with the experimental system.

2. In addition, hydrodynamic correction factors were not incorporated in the theoretical model for the sake of a simplified approach. Including the hydrodynamic correction factors could provide a more rigorous working model and lead to better predictions of particle behavior [Molla, 2004].

3. In spite of considering a suitably dilute suspension, pearl chaining due to inter-particle interactions have been observed in the experiments. This leads one to conclude that, the inter-particle interactions may play an important role in describing the overall behavior of the particles and can be an interesting starting point for further analysis.

Bibliography

Andritsos, N., Kontopoulou, M., Karabelas, A.J., and Koutsoukos, P.G. Calcium carbonate deposit formation under isothermal conditions. *Canadian Journal of Chemical Engineering*, 74:911–919, 1996.

Ascher, U.M. and Petzold, L.R. *Computer Methods for Ordinary Differential Equations and Differential-Algebraic-Equations*. SIAM: Society for Industrial and Applied Mathematics; illustrated edition (1998), 1998.

Baker, J.S. and Dudley, L.Y. Biofouling in membrane systems - a review. *Desalination*, 118:81–90, 1998.

Baker, J.S. and Judd, S.J. Magnetic amelioration of scale formation. *Water Research*, 30:247–260, 1996.

Banerjee, I., Pangule, R.C., and Kane, R.S. Antifouling coatings: Recent developments in the design of surfaces that prevent fouling by proteins, bacteria, and marine organisms. *Advanced Materials*, 23:690–718, 2011.

Bansal, B. and Muller, H. Crystallization fouling in plate heat exchangers. *ASME Journal of Heat Transfer*, 115:584–591, 1993.

Barbulovic, I., Yang, H., Park, P.S., and Wheeler, A.R. Digital microfluidics for cell-based assays. *Lab on a Chip - Miniaturisation for Chemistry and Biology*, 8:519–526, 2008.

Bazaka, K., Jacob, M.V., Crawford, R.J., and Ivanova, E.P. Plasma-assisted surface modification of organic biopolymers to prevent bacterial attachment. *Acta Biomaterialia*, 7:2015–2028, 2011.

Bell K.J. and Mueller A.C. Wolverine engineering data book ii, 2001. URL `http://www.wlv.com/products/databook/databook.pdf`Taken on August 25, 2011.

Bhattacharjee, S. and Johnston, G.M. A model of membrane fouling by salt precipitation from multicomponent ionic mixtures in crossflow nanofiltration. *Environmental Engineering Science*, 19:399–412, 2002.

Bhattacharjee, S., Kim, A.S., and Elimelech, M. Concentration polarization of interacting solute particles in cross-flow membrane filtration. *Journal of Colloid and Interface Science*, 212:81–99, 1999.

Bhattacharjee, S., Chen, J.C., and Elimelech, M. Coupled model of concentration polarization and pore transport in crossflow nanofiltration. *AIChE Journal*, 47:2733–2745, 2001.

Bico, J., Thiele, U., and Quere, D. Wetting of textured surfaces. *Colloids and Surfaces A: Physicochemical and Engineering Aspects*, 206:41–46, 2002.

Boussu, K., Belpaire, A., Volodin, A., Van Haesendonck, C., Van der Meeren, P., Vandecasteele C., and Van der Bruggen B. Influence of membrane and colloid characteristics on fouling of nanofiltration membranes. *Journal of Membrane Science*, 289:220–230, 2007.

Brenan and Kathryn Eleda. *Numerical solution of initial-value problems in differential-algebraic equations*. North-Holland, 1989.

Chang, F.C. and Su, Y.C. Controlled double emulsification utilizing 3d pdms microchannels. *Journal of Micromechanics and Microengineering*, 18, 2008.

Chen, V., Fane, A.G., Madaeni, S., and Wenten, I.G. Particle deposition during membrane filtration of colloids: Transition between concentration polarization and cake formation. *Journal of Membrane Science*, 125:109–122, 1997.

Cho, Y.I., Fan, C., and Choi, B.G. Theory of electronic anti-fouling technology to control precipitation fouling in heat exchangers. *International Communications in Heat and Mass Transfer*, 24:757–770, 1997.

Cho, Y.I., Fridman, A.F., Lee, S.H., and Kim, W.T. Physical water treatment for fouling prevention in heat exchangers. *Advances in Heat Transfer*, 38: 1–72, 2004.

Chong, T.H. and Fane, A.G. Implications of critical flux and cake enhanced osmotic pressure (ceop) on colloidal fouling in reverse osmosis: Modeling approach. *Desalination and Water Treatment*, 8:68–90, 2009.

Chong, T.H., Wong, F.S., and Fane, A.G. Implications of critical flux and cake enhanced osmotic pressure (ceop) on colloidal fouling in reverse osmosis: Experimental observations. *Journal of Membrane Science*, 314:101–111, 2008.

Clague, D.S. and Wheeler, E.K. Dielectrophoretic manipulation of macromolecules: The electric field *Physical Review E*, 64: art. no.-026605, 2001.

Crews, N., Darabi, J., Voglewede, P., Guo, F., and Bayoumi, A. An analysis of interdigitated electrode geometry for dielectrophoretic particle transport in micro-fluidics. *Sensors and Actuators B-Chemical*, 125:672–679, 2007.

Dalas, E. and Koutsoukos, P.G. Calcium carbonate scale formation and prevention in a flow-through system at various temperatures. *Desalination*, 78: 403–416, 1990.

Dhanasekaran, D., Thajuddin, N., Rashmi, M., Deepika, T.L., and Gunasekaran, M. Screening of biofouling activity in marine bacterial isolate from ship hull. *International Journal of Membrane Science and Technology*, 6:197–202, 2009.

Dobretsov, S., Dahms, H.U., and Qian, P.Y. Inhibition of biofouling by marine microorganisms and their metabolites. *Biofouling*, 22:43–54, 2006.

Dobretsov, S., Teplitski, M., and Paul, V. Mini-review: Quorum sensing in the marine environment and its relationship to biofouling. *Biofouling*, 25: 413–427, 2009.

Dowling, D.P., Nwankire, C.E., Riihimki, M., Keiski, R., and Nylan, U. Evaluation of the anti-fouling properties of nm thick atmospheric plasma deposited coatings. *Surface and Coatings Technology*, 205:1544–1551, 2010.

Du, F., Hawari, A., Baune, M., and Thoeming, J. Dielectrophoretically intensified cross-flow membrane filtration. *Journal of Membrane Science*, 336: 71–78, 2009.

Elimelech, M., Jia, X., Gregory, J., and Williams, R. *Particle Deposition & Aggregation: Measurement, Modeling and Simulation*. Butterworth Heinemann, 1995.

Epstein, N. *Fouling of heat exchangers*. Hemisphere Publishing Corporation, Washington, DC, USA, 1986.

Epstein, N. Elements of particle deposition onto nonporous solid surfaces parallel to suspension flows. *Experimental Thermal and Fluid Science*, 14: 323–334, 1997.

Falconnet, D., Csucs, G., Michelle, H., and Textor, M. Surface engineering approaches to micropattern surfaces for cell-based assays. *Biomaterials*, 27: 3044–3063, 2006.

Fan, L., Nguyen, T., Roddick, F.A., and Harris, J.L. Low-pressure membrane filtration of secondary effluent in water reuse: Pre-treatment for fouling reduction. *Journal of Membrane Science*, 320:135–142, 2008.

Feng, D., Deventer, V.J., and Aldrich, C. Ultrasonic defouling of reverse osmosis membranes used to treat wastewater effluents. *Separation and Purification Technology*, 50:318–323, 2006.

Flemming, H.C. Biofilms and environmental protection. *Water Science and Technology*, 27:1–10, 1993.

Gao, W., Liang, H., Ma, J., Han, M., Chen, Z.L., Han, Z.S., and Li, G.B. Membrane fouling control in ultrafiltration technology for drinking water production: A review. *Desalination*, 272:1–8, 2011.

Gascoyne, P.R.C., Noshari, J., Anderson, T.J., and Becker, F.F. Isolation of rare cells from cell mixtures by dielectrophoresis. *Electrophoresis*, 30: 1388–1398, 2009.

Hasson, D. and Zahavi, J. Mechanism of calcium sulfate scale deposition on heat-transfer surfaces. *Industrial and Engineering Chemistry Fundamentals*, 9:1–10, 1970.

Hu, Y., Hadziomerspahic, A., and Wang, Y. Role of surfactants in suppressing aging of silica-poly(dimethylsiloxane) gels. *Macromolecules*, 43:8233–8238, 2010.

Huang, Y., Wang, X.B., Becker, F.F., and Gascoyne, P.R.C. Introducing dielectrophoresis as a new force field for field-flow fractionation. *Biophysical Journal*, 73:1118–1129, 1997.

Jelvestam, M., Edrud, S., Petronis, S., and Gatenholm, P. Biomimetic materials with tailored surface micro-architecture for prevention of marine biofouling. *Surface and Interface Analysis*, 35:168–173, 2003.

Jones, T.B. *Electromechanics of Particles*. Cambridge University Press, 1995.

Katsoufidou, K., Yiantsios, S.G., and Karabelas, A.J. An experimental study of uf membrane fouling by humic acid and sodium alginate solutions: the effect of backwashing on flux recovery. *Desalination*, 220:214–227, 2008.

Kazi, S.N., Duffy, G.G., and Chen, X.D. Mineral scale formation and mitigation on metals and a polymeric heat exchanger surface. *Applied Thermal Engineering*, 30:2236–2242, 2010.

Kim, A.S., Contreras, A.E., Li, Q., and Yuan, R. Fundamental mechanisms of three-component combined fouling with experimental verification. *Langmuir*, 25:7815–7827, 2009.

Kobayashi, T., Hosaka, Y., and Fujii, N. Ultrasound-enhanced membrane-cleaning processes applied water treatments: influence of sonic frequency on filtration treatments. *Ultrasonics*, 41:185–190, 2003.

Kwak, S.Y., Kim, S.H., and Kim, S.S. Hybrid organic/inorganic reverse osmosis (ro) membrane for bactericidal anti-fouling. 1. preparation and characterization of tio2 nanoparticle self-assembled aromatic polyamide thin-film-composite (tfc) membrane. *Environmental Science and Technology*, 35: 2388–2394, 2001.

Kyllonen, H.M., Pirkonen, P., and Nystrom, M. Membrane filtration enhanced by ultrasound: A review. *Desalination*, 181:319–335, 2005.

Lapizco, B.H., Simmons, B.A., Cummings, E.B., and Fintschenko, Y. Insulator-based dielectrophoresis for the selective concentration and separation of live bacteria in water. *Electrophoresis*, 25:1695–1704, 2004.

Lauga, E. and Powers, T.R. The hydrodynamics of swimming microorganisms. *Rep. Prog. Phys.*, 72:096601, 2009.

Lee, S.H. and Cho, Y.I. Study of the performance of physical water treatment with a solenoid coil to prevent mineral fouling. part 1: Effect of a side-stream filtration. *International Communications in Heat and Mass Transfer*, 29: 145–156, 2002.

Lee, W., Ahn, C.H., Hong, S., Kim, S., Lee, S., Baek, Y., and Yoon, J. Evaluation of surface properties of reverse osmosis membranes on the initial biofouling stages under no filtration condition. *Journal of Membrane Science*, 351:112–122, 2010.

Li, Q. and Elimelech, M. Synergistic effects in combined fouling of a loose nanofiltration membrane by colloidal materials and natural organic matter. *Journal of Membrane Science*, 278:72–82, 2006.

Liu, C.X., Zhang, D.R., He, Y., Zhao, X.S., and Bai, R. Modification of membrane surface for anti-biofouling performance: Effect of anti-adhesion and anti-bacteria approaches. *Journal of Membrane Science*, 346:121–130, 2010.

Liu, R. and Cho, Y.I. Combined use of an electronic antifouling technology and brush punching for scale removal in a water-cooled plain tube. *Experimental Heat Transfer*, 12:203–213, 1999.

Magin, C.M., Cooper, S.P., and Brennan, A.B. Non-toxic antifouling strategies. *Materials Today*, 13:36–44, 2010.

Markx, G.H., Pethig, R., and Rousselet, J. The dielectrophoretic levitation of latex beads, with reference to field-flow fractionation. *Journal of Physics D: Applied Physics*, 30:2470–2477, 1997.

Melo, L.F., Bott, T.R., and Bernardo, C.A. *Fouling science and technology*. Springer, 1988.

Molla, S. Dielectrophoretic membrane filtration. Master's thesis, University of Alberta, 2004.

Molla, S. and Bhattacharjee, S. Prevention of colloidal membrane fouling employing dielectrophoretic forces on a parallel electrode array. *Journal of Membrane Science*, 255:187–199, 2005.

Molla, S. and Bhattacharjee, S. Dielectrophoretic levitation in the presence of shear flow: Implications for colloidal fouling of filtration membranes. *Langmuir*, 23:10618–10627, 2007.

Morgan, H. and Green, N.G. *AC Electrokinetics: Colloids and Nanoparticles*. Research Studies Press Ltd., 2003.

Ning, R.Y. and Troyer, T.L. Colloidal fouling of ro membranes following mf/uf in the reclamation of municipal wastewater. *Desalination*, 208:232–237, 2007.

Peng, H., Alvarez, N.T., Kittrell, C., Hauge, R.H., and Schmidt, H.K. Dielectrophoresis field flow fractionation of single-walled carbon nanotubes. *Journal of the American Chemical Society*, 128:8396–8397, 2006.

Pohl, H. *Dielectrophoresis*. Cambridge University Press, 1978.

Popat, K.C and Desai, T.A. Poly(ethylene glycol) interfaces: an approach for enhanced performance of microfluidic systems. *Biosensors and Bioelectronics*, 19:1037–1044, 2004.

Qamar, A., Wong, Z.Z., Fowlkes, J.B., and Bull, J.L. Dynamics of acoustic droplet vaporization in gas embolotherapy. *Applied Physics Letters*, 96, 2010.

Rosenhahn, A., Schilp, S., Kreuzer, H.J., and Grunze, M. The role of "inert" surface chemistry in marine biofouling prevention. *Physical Chemistry Chemical Physics*, 12:4275–4286, 2010.

Rousselet, J., Markx, G.H., and Pethig, R. Separation of erythrocytes and latex beads by dielectrophoretic levitation and hyperlayer field-flow fractionation. *Colloids and Surfaces A: Physicochemical and Engineering Aspects*, 140:209–216, 1998.

Sanchis, A., Brown, A.P., Sancho, M., Martinez, G., Sebastian, J.L., Munoz, S., and Miranda, J.M. Dielectric characterization of bacterial cells using dielectrophoresis. *Bioelectromagnetics*, 28:393–401, 2007.

Santini, J.T., Richards, A.C., Scheidt, R., Cima, M.J., and Langer, R. Microchips as controlled drug-delivery devices. *Angewandte Chemie - International Edition*, 39:2396–2407, 2000.

Sheikholeslami, R. Calcium sulfate fouling-precipitation or participate: A proposed composite model. *Heat Transfer Engineering*, 21:24–33, 2000.

Sheikholeslami, R. and Tan, S. Effects of water quality on silica fouling of desalination plants. *Desalination*, 126:267–280, 1999.

Shirazi, S., Lin, C.J., and Chen, D. Inorganic fouling of pressure-driven membrane processes - a critical review. *Desalination*, 250:236–248, 2010.

Smith, P.J., Shon, H.K., Vigneswaran, S., Ngo, H.H., and Nguyen, H. Productivity enhancement in a cross-flow ultrafiltration membrane system through automated de-clogging operations. *Journal of Membrane Science*, 280:82–88, 2006.

Sohn, C.H., Kim, C.S., Moon, S.Y., and Cho, Y.I. Effect of a longitudinally positioned solenoid coil on electronic descaling. *International Communications in Heat and Mass Transfer*, 32(1-2):240–247, 2005.

Somerscales, E.F.C. and Knudsen, J.G. *Fouling of heat transfer equipment*. Hemisphere Pub. Corp., 1981.

Somerscales, E.F.C. Fouling of heat transfer surfaces: an historical review. *Heat Transfer Engineering*, 11:19–36, 1990.

Srivastava, S.K., Gencoglu, A., and Minerick, A.R. Dc insulator dielectrophoretic applications in microdevice technology: A review. *Analytical and Bioanalytical Chemistry*, 399:301–321, 2011.

Suehiro, J., Ikeda, N., Ohtsubo, A., and Imasaka, K. Fabrication of bio/-nano interfaces between biological cells and carbon nanotubes using dielectrophoresis. *Microfluidics and Nanofluidics*, 5:741–747, 2008.

Tan, S.H., Nguyen, N.T., Chua, Y.C., and Kang, T.G. Oxygen plasma treatment for reducing hydrophobicity of a sealed polydimethylsiloxane microchannel. *Biomicrofluidics*, 4:1–8, 2010.

Tang, C.Y., Kwon, Y.N., and Leckie, J.O. The role of foulant-foulant electrostatic interaction on limiting flux for ro and nf membranes during humic acid fouling-theoretical basis, experimental evidence, and afm interaction force measurement. *Journal of Membrane Science*, 326:526–532, 2009.

Tang, C.Y., Chong, T.H., and Fane, A.G. Colloidal interactions and fouling of nf and ro membranes: A review. *Advances in Colloid and Interface Science*, 164:126–143, 2011.

Turner, C.W. and Lister, D.H. Study of the deposition of silt onto the surface of type 304 stainless steel. *Canadian Journal of Chemical Engineering*, 69: 203–211, 1991.

Hulle, S.W.H. , Vergote, A., Hogie, J., and Dejans, P. Practical assessment of electronic water treatment for the prevention of fouling. *Chemical Engineering and Technology*, 30:659–662, 2007.

Veerasamy, D., Supurmaniam, A., and Nor, Z.M. Evaluating the use of in-situ ultrasonication to reduce fouling during natural rubber skim latex (waste latex) recovery by ultrafiltration. *Desalination*, 236:202–207, 2009.

Wakizaka, Y., Hakoda, M., and Shiragami, N. Effect of electrode geometry on dielectrophoretic separation of cells. *Biochemical Engineering Journal*, 20: 13–19, 2004.

Wang, Y.N. and Tang, C.Y. Protein fouling of nanofiltration, reverse osmosis, and ultrafiltration membranes-the role of hydrodynamic conditions, solution chemistry, and membrane properties. *Journal of Membrane Science*, 376: 275–282, 2011.

Wei, X., Wang, Z., Chen, J., Wang, J., and Wang, S. A novel method of surface modification on thin-film-composite reverse osmosis membrane by grafting hydantoin derivative. *Journal of Membrane Science*, 346:152–162, 2010.

Wisniewski, N. and Reichert, M. Methods for reducing biosensor membrane biofouling. *Colloids and Surfaces B: Biointerfaces*, 18:197–219, 2000.

Xiong, Y. and Liu, Y. Biological control of microbial attachment: A promising alternative for mitigating membrane biofouling. *Applied Microbiology and Biotechnology*, 86:825–837, 2010.

Yang, F., Yang, X., Jiang, H., Bulkhaults, P., Wood, P., Hrushesky, W., and Wang, G. Dielectrophoretic separation of colorectal cancer cells. *Biomicrofluidics*, 4:1–13, 2010.

Yang, H.L., Lin, J.C.T., and Huang, C. Application of nanosilver surface modification to ro membrane and spacer for mitigating biofouling in seawater desalination. *Water Research*, 43:3777–3786, 2009.

Yigit, N.O., Civelekoglu, G., Harman, I., Koseoglu, H., and Kitis, M. Effects of various backwash scenarios on membrane fouling in a membrane bioreactor. *Desalination*, 237:346–356, 2009.

Yu, H., Sheikholeslami, R., and Doherty, W.O.S. Composite fouling characteristics of calcium oxalate monohydrate and amorphous silica by a novel approach simulating successive effects of a sugar mill evaporator. *Industrial and Engineering Chemistry Research*, 41:3379–3388, 2002.

Zdaniuk, G.J., Chamra, L.M., and Mago, P.J. A literature survey of water-side fouling applicable to cooling tower condensers. *Proceedings of the Institution of Mechanical Engineers, Part A: Journal of Power and Energy*, 220:815–827, 2006.

Zhao, C., Burchardt, M., Brinkhoff, T., Beardsley, C., Simon M., and Wittstock, G. Microfabrication of patterns of adherent marine bacterium phaeobacter inhibens using soft lithography and scanning probe lithography. *Langmuir*, 26:8641–8647, 2010.

Appendix A

Table A.1 – Electrical, Geometric and Hydrodynamic properties of Single and Multi-component Colloidal System

Property	Value
Electrode gap	25 and 50 μm
Electrode width	25 and 50 μ m
Relative permittivity of medium	80
pH of the suspension	7.1
Conductivity of DI water	18.2 MOhm-cm
Conductivity of the suspension	4 μS/cm
Range of applied voltage	1-10 V
Frequency of applied signal	500 Hz-1 MHz
Channel Height	1 mm
Channel width	20 mm
Number Concentration of the suspension	2.1 $\times 10^6$ /ml
Average cross flow velocity	1.4×10^{-6} m/s